

Determination of U-spin breaking parameters with an amplitude analysis of the decay $D^0 \rightarrow K_L^0 \pi^+ \pi^-$

The BESIII collaboration

E-mail: besiii-publications@ihep.ac.cn

ABSTRACT: We present a study of the resonant structure of the decay $D^0 \rightarrow K_L^0 \pi^+ \pi^-$, using quantum-correlated $D^0 \bar{D}^0$ data produced at $\sqrt{s} = 3.773$ GeV. The data sample was collected by the BESIII experiment and corresponds to an integrated luminosity of 2.93 fb^{-1} . This study is the first amplitude analysis of a decay mode involving a K_L^0 , which also results in the first measurement of the complex *U-spin breaking parameters* ($\hat{\rho}$) related to various *CP*-eigenstate resonant modes through which the three-body decay proceeds. The moduli of the $\hat{\rho}$ parameters have central values in a wide range from 0.4 to 12.1, which indicates substantial U-spin symmetry breaking. We present the fractional resonant contributions and average strong-phase parameters over regions of phase space for both $K_S^0 \pi^+ \pi^-$ and $K_L^0 \pi^+ \pi^-$ modes. We also report the ratio of the branching fractions between $K_L^0 \pi^+ \pi^-$ and $K_S^0 \pi^+ \pi^-$ decay modes and the *CP*-even fraction of the $K_L^0 \pi^+ \pi^-$ state calculated using the U-spin breaking parameters.

Contents

1	Introduction	8
2	Strong-phase and amplitude-analysis formalism	9
3	BESIII detector and simulated sample	16
4	Event selection	17
5	Amplitude analysis	21
6	Results	27
7	Systematic uncertainty	30
8	CP content and BF ratio	31
9	Conclusion	32
A	Angular dependence of Breit-Wigner amplitude in $D \rightarrow PV$ decays	34
B	Fits performed on individual tag-mode event samples separately	35
C	Standalone $K_L^0 \pi^+ \pi^-$ fit	36
D	Systematic source-wise break up	38
E	Predicted and assumed $\Delta c_i, \Delta s_i$	43

M. Ablikim¹, M. N. Achasov^{12,b}, P. Adlarson⁷², R. Aliberti³³, A. Amoroso^{71A,71C},
M. R. An³⁷, Q. An^{68,55}, Y. Bai⁵⁴, O. Bakina³⁴, R. Baldini Ferroli^{27A}, I. Balossino^{28A},
Y. Ban^{44,g}, V. Batozskaya^{1,42}, D. Becker³³, K. Begzsuren³⁰, N. Berger³³, M. Bertani^{27A},
D. Bettoni^{28A}, F. Bianchi^{71A,71C}, E. Bianco^{71A,71C}, J. Bloms⁶⁵, A. Bortone^{71A,71C},
I. Boyko³⁴, R. A. Briere⁵, A. Brueggemann⁶⁵, H. Cai⁷³, X. Cai^{1,55}, A. Calcaterra^{27A},
G. F. Cao^{1,60}, N. Cao^{1,60}, S. A. Cetin^{59A}, J. F. Chang^{1,55}, W. L. Chang^{1,60}, G. R. Che⁴¹,
G. Chelkov^{34,a}, C. Chen⁴¹, Chao Chen⁵², G. Chen¹, H. S. Chen^{1,60}, M. L. Chen^{1,55,60},
S. J. Chen⁴⁰, S. M. Chen⁵⁸, T. Chen^{1,60}, X. R. Chen^{29,60}, X. T. Chen^{1,60}, Y. B. Chen^{1,55},
Y. Q. Chen³², Z. J. Chen^{24,h}, W. S. Cheng^{71C}, S. K. Choi⁵², X. Chu⁴¹, G. Cibinetto^{28A},
S. C. Coen⁴, F. Cossio^{71C}, J. J. Cui⁴⁷, H. L. Dai^{1,55}, J. P. Dai⁷⁶, A. Dbeyssi¹⁸, R. E. de
Boer⁴, D. Dedovich³⁴, Z. Y. Deng¹, A. Denig³³, I. Denysenko³⁴, M. Destefanis^{71A,71C},
F. De Mori^{71A,71C}, Y. Ding³², Y. Ding³⁸, J. Dong^{1,55}, L. Y. Dong^{1,60}, M. Y. Dong^{1,55,60},
X. Dong⁷³, S. X. Du⁷⁸, Z. H. Duan⁴⁰, P. Egorov^{34,a}, Y. L. Fan⁷³, J. Fang^{1,55},
S. S. Fang^{1,60}, W. X. Fang¹, Y. Fang¹, R. Farinelli^{28A}, L. Fava^{71B,71C}, F. Feldbauer⁴,
G. Felici^{27A}, C. Q. Feng^{68,55}, J. H. Feng⁵⁶, K. Fischer⁶⁶, M. Fritsch⁴, C. Fritzsche⁶⁵,
C. D. Fu¹, Y. W. Fu¹, H. Gao⁶⁰, Y. N. Gao^{44,g}, Yang Gao^{68,55}, S. Garbolino^{71C},
I. Garzia^{28A,28B}, P. T. Ge⁷³, Z. W. Ge⁴⁰, C. Geng⁵⁶, E. M. Gersabeck⁶⁴, A. Gilman⁶⁶,
K. Goetzen¹³, L. Gong³⁸, W. X. Gong^{1,55}, W. Gradl³³, M. Greco^{71A,71C}, M. H. Gu^{1,55},
Y. T. Gu¹⁵, C. Y. Guan^{1,60}, Z. L. Guan²¹, A. Q. Guo^{29,60}, L. B. Guo³⁹, R. P. Guo⁴⁶,
Y. P. Guo^{11,f}, A. Guskov^{34,a}, X. T. H.^{1,60}, W. Y. Han³⁷, X. Q. Hao¹⁹, F. A. Harris⁶²,
K. K. He⁵², K. L. He^{1,60}, F. H. Heinsius⁴, C. H. Heinz³³, Y. K. Heng^{1,55,60}, C. Herold⁵⁷,
T. Holtmann⁴, G. Y. Hou^{1,60}, Y. R. Hou⁶⁰, Z. L. Hou¹, H. M. Hu^{1,60}, J. F. Hu^{53,i},
T. Hu^{1,55,60}, Y. Hu¹, G. S. Huang^{68,55}, K. X. Huang⁵⁶, L. Q. Huang^{29,60}, X. T. Huang⁴⁷,
Y. P. Huang¹, T. Hussain⁷⁰, N. Hüsken^{26,33}, W. Imoehl²⁶, M. Irshad^{68,55}, J. Jackson²⁶,
S. Jaeger⁴, S. Janchiv³⁰, E. Jang⁵², J. H. Jeong⁵², Q. Ji¹, Q. P. Ji¹⁹, X. B. Ji^{1,60},
X. L. Ji^{1,55}, Y. Y. Ji⁴⁷, Z. K. Jia^{68,55}, P. C. Jiang^{44,g}, S. S. Jiang³⁷, T. J. Jiang¹⁶,
X. S. Jiang^{1,55,60}, Y. Jiang⁶⁰, J. B. Jiao⁴⁷, Z. Jiao²², S. Jin⁴⁰, Y. Jin⁶³, M. Q. Jing^{1,60},
T. Johansson⁷², X. K.¹, S. Kabana³¹, N. Kalantar-Nayestanaki⁶¹, X. L. Kang⁹,
X. S. Kang³⁸, R. Kappert⁶¹, M. Kavatsyuk⁶¹, B. C. Ke⁷⁸, A. Khoukaz⁶⁵, R. Kiuchi¹,
R. Kliemt¹³, L. Koch³⁵, O. B. Kolcu^{59A}, B. Kopf⁴, M. Kuessner⁴, A. Kupsc^{42,72},
W. Kühn³⁵, J. J. Lane⁶⁴, J. S. Lange³⁵, P. Larin¹⁸, A. Lavania²⁵, L. Lavezzi^{71A,71C},
T. T. Lei^{68,k}, Z. H. Lei^{68,55}, H. Leithoff³³, M. Lellmann³³, T. Lenz³³, C. Li⁴¹, C. Li⁴⁵,
C. H. Li³⁷, Cheng Li^{68,55}, D. M. Li⁷⁸, F. Li^{1,55}, G. Li¹, H. Li^{68,55}, H. B. Li^{1,60}, H. J. Li¹⁹,
H. N. Li^{53,i}, Hui Li⁴¹, J. R. Li⁵⁸, J. S. Li⁵⁶, J. W. Li⁴⁷, Ke Li¹, L. J. Li^{1,60}, L. K. Li¹,
Lei Li³, M. H. Li⁴¹, P. R. Li^{36,j,k}, S. X. Li¹¹, S. Y. Li⁵⁸, T. Li⁴⁷, W. D. Li^{1,60}, W. G. Li¹,
X. H. Li^{68,55}, X. L. Li⁴⁷, Xiaoyu Li^{1,60}, Y. G. Li^{44,g}, Z. J. Li⁵⁶, Z. X. Li¹⁵, Z. Y. Li⁵⁶,
C. Liang⁴⁰, H. Liang^{1,60}, H. Liang^{68,55}, H. Liang³², Y. F. Liang⁵¹, Y. T. Liang^{29,60},
G. R. Liao¹⁴, L. Z. Liao⁴⁷, J. Libby²⁵, A. Limphirat⁵⁷, D. X. Lin^{29,60}, T. Lin¹,
B. X. Liu⁷³, B. J. Liu¹, C. Liu³², C. X. Liu¹, D. Liu^{18,68}, F. H. Liu⁵⁰, Fang Liu¹,
Feng Liu⁶, G. M. Liu^{53,i}, H. Liu^{36,j,k}, H. B. Liu¹⁵, H. M. Liu^{1,60}, Huanhuan Liu¹,
Huihui Liu²⁰, J. B. Liu^{68,55}, J. L. Liu⁶⁹, J. Y. Liu^{1,60}, K. Liu¹, K. Y. Liu³⁸, Ke Liu²¹,
L. Liu^{68,55}, L. C. Liu²¹, Lu Liu⁴¹, M. H. Liu^{11,f}, P. L. Liu¹, Q. Liu⁶⁰, S. B. Liu^{68,55},
T. Liu^{11,f}, W. K. Liu⁴¹, W. M. Liu^{68,55}, X. Liu^{36,j,k}, Y. Liu^{36,j,k}, Y. B. Liu⁴¹,

Z. A. Liu^{1,55,60}, Z. Q. Liu⁴⁷, X. C. Lou^{1,55,60}, F. X. Lu⁵⁶, H. J. Lu²², J. G. Lu^{1,55},
 X. L. Lu¹, Y. Lu⁷, Y. P. Lu^{1,55}, Z. H. Lu^{1,60}, C. L. Luo³⁹, M. X. Luo⁷⁷, T. Luo^{11,f},
 X. L. Luo^{1,55}, X. R. Lyu⁶⁰, Y. F. Lyu⁴¹, F. C. Ma³⁸, H. L. Ma¹, J. L. Ma^{1,60}, L. L. Ma⁴⁷,
 M. M. Ma^{1,60}, Q. M. Ma¹, R. Q. Ma^{1,60}, R. T. Ma⁶⁰, X. Y. Ma^{1,55}, Y. Ma^{44,g},
 F. E. Maas¹⁸, M. Maggiora^{71A,71C}, S. Maldaner⁴, S. Malde⁶⁶, Q. A. Malik⁷⁰,
 A. Mangoni^{27B}, Y. J. Mao^{44,g}, Z. P. Mao¹, S. Marcello^{71A,71C}, Z. X. Meng⁶³,
 J. G. Messchendorp^{13,61}, G. Mezzadri^{28A}, H. Miao^{1,60}, T. J. Min⁴⁰, R. E. Mitchell²⁶,
 X. H. Mo^{1,55,60}, N. Yu. Muchnoi^{12,b}, Y. Nefedov³⁴, F. Nerling^{18,d}, I. B. Nikolaev^{12,b},
 Z. Ning^{1,55}, S. Nisar^{10,l}, Y. Niu⁴⁷, S. L. Olsen⁶⁰, Q. Ouyang^{1,55,60}, S. Pacetti^{27B,27C},
 X. Pan⁵², Y. Pan⁵⁴, A. Pathak³², Y. P. Pei^{68,55}, M. Pelizaeus⁴, H. P. Peng^{68,55},
 K. Peters^{13,d}, J. L. Ping³⁹, R. G. Ping^{1,60}, S. Plura³³, S. Pogodin³⁴, V. Prasad^{68,55},
 F. Z. Qi¹, H. Qi^{68,55}, H. R. Qi⁵⁸, M. Qi⁴⁰, T. Y. Qi^{11,f}, S. Qian^{1,55}, W. B. Qian⁶⁰,
 Z. Qian⁵⁶, C. F. Qiao⁶⁰, J. J. Qin⁶⁹, L. Q. Qin¹⁴, X. P. Qin^{11,f}, X. S. Qin⁴⁷, Z. H. Qin^{1,55},
 J. F. Qiu¹, S. Q. Qu⁵⁸, K. H. Rashid⁷⁰, C. F. Redmer³³, K. J. Ren³⁷, A. Rivetti^{71C},
 V. Rodin⁶¹, M. Rolo^{71C}, G. Rong^{1,60}, Ch. Rosner¹⁸, S. N. Ruan⁴¹, A. Sarantsev^{34,c},
 Y. Schelhaas³³, K. Schoenning⁷², M. Scodreggio^{28A,28B}, K. Y. Shan^{11,f}, W. Shan²³,
 X. Y. Shan^{68,55}, J. F. Shangguan⁵², L. G. Shao^{1,60}, M. Shao^{68,55}, C. P. Shen^{11,f},
 H. F. Shen^{1,60}, W. H. Shen⁶⁰, X. Y. Shen^{1,60}, B. A. Shi⁶⁰, H. C. Shi^{68,55}, J. Y. Shi¹,
 Q. Q. Shi⁵², R. S. Shi^{1,60}, X. Shi^{1,55}, J. J. Song¹⁹, T. Z. Song⁵⁶, W. M. Song^{32,1},
 Y. X. Song^{44,g}, S. Sosio^{71A,71C}, S. Spataro^{71A,71C}, F. Stieler³³, Y. J. Su⁶⁰, G. B. Sun⁷³,
 G. X. Sun¹, H. Sun⁶⁰, H. K. Sun¹, J. F. Sun¹⁹, K. Sun⁵⁸, L. Sun⁷³, S. S. Sun^{1,60},
 T. Sun^{1,60}, W. Y. Sun³², Y. Sun⁹, Y. J. Sun^{68,55}, Y. Z. Sun¹, Z. T. Sun⁴⁷, Y. X. Tan^{68,55},
 C. J. Tang⁵¹, G. Y. Tang¹, J. Tang⁵⁶, Y. A. Tang⁷³, L. Y. Tao⁶⁹, Q. T. Tao^{24,h}, M. Tat⁶⁶,
 J. X. Teng^{68,55}, V. Thoren⁷², W. H. Tian⁴⁹, W. H. Tian⁵⁶, Y. Tian^{29,60}, Z. F. Tian⁷³,
 I. Uman^{59B}, B. Wang¹, B. Wang^{68,55}, B. L. Wang⁶⁰, C. W. Wang⁴⁰, D. Y. Wang^{44,g},
 F. Wang⁶⁹, H. J. Wang^{36,j,k}, H. P. Wang^{1,60}, K. Wang^{1,55}, L. L. Wang¹, M. Wang⁴⁷,
 Meng Wang^{1,60}, S. Wang^{11,f}, T. Wang^{11,f}, T. J. Wang⁴¹, W. Wang⁵⁶, W. Wang⁶⁹,
 W. H. Wang⁷³, W. P. Wang^{68,55}, X. Wang^{44,g}, X. F. Wang^{36,j,k}, X. J. Wang³⁷,
 X. L. Wang^{11,f}, Y. Wang⁵⁸, Y. D. Wang⁴³, Y. F. Wang^{1,55,60}, Y. H. Wang⁴⁵,
 Y. N. Wang⁴³, Y. Q. Wang¹, Yaqian Wang^{17,1}, Yi Wang⁵⁸, Z. Wang^{1,55}, Z. L. Wang⁶⁹,
 Z. Y. Wang^{1,60}, Ziyi Wang⁶⁰, D. Wei⁶⁷, D. H. Wei¹⁴, F. Weidner⁶⁵, S. P. Wen¹,
 C. W. Wenzel⁴, D. J. White⁶⁴, U. Wiedner⁴, G. Wilkinson⁶⁶, M. Wolke⁷², L. Wollenberg⁴,
 C. Wu³⁷, J. F. Wu^{1,60}, L. H. Wu¹, L. J. Wu^{1,60}, X. Wu^{11,f}, X. H. Wu³², Y. Wu⁶⁸,
 Y. J. Wu²⁹, Z. Wu^{1,55}, L. Xia^{68,55}, X. M. Xian³⁷, T. Xiang^{44,g}, D. Xiao^{36,j,k}, G. Y. Xiao⁴⁰,
 H. Xiao^{11,f}, S. Y. Xiao¹, Y. L. Xiao^{11,f}, Z. J. Xiao³⁹, C. Xie⁴⁰, X. H. Xie^{44,g}, Y. Xie⁴⁷,
 Y. G. Xie^{1,55}, Y. H. Xie⁶, Z. P. Xie^{68,55}, T. Y. Xing^{1,60}, C. F. Xu^{1,60}, C. J. Xu⁵⁶,
 G. F. Xu¹, H. Y. Xu⁶³, Q. J. Xu¹⁶, X. P. Xu⁵², Y. C. Xu⁷⁵, Z. P. Xu⁴⁰, F. Yan^{11,f},
 L. Yan^{11,f}, W. B. Yan^{68,55}, W. C. Yan⁷⁸, X. Q. Yan¹, H. J. Yang^{48,e}, H. L. Yang³²,
 H. X. Yang¹, Tao Yang¹, Y. F. Yang⁴¹, Y. X. Yang^{1,60}, Yifan Yang^{1,60}, M. Ye^{1,55},
 M. H. Ye⁸, J. H. Yin¹, Z. Y. You⁵⁶, B. X. Yu^{1,55,60}, C. X. Yu⁴¹, G. Yu^{1,60}, T. Yu⁶⁹,
 X. D. Yu^{44,g}, C. Z. Yuan^{1,60}, L. Yuan², S. C. Yuan¹, X. Q. Yuan¹, Y. Yuan^{1,60},
 Z. Y. Yuan⁵⁶, C. X. Yue³⁷, A. A. Zafar⁷⁰, F. R. Zeng⁴⁷, X. Zeng^{11,f}, Y. Zeng^{24,h},
 X. Y. Zhai³², Y. H. Zhan⁵⁶, A. Q. Zhang^{1,60}, B. L. Zhang^{1,60}, B. X. Zhang¹,

D. H. Zhang⁴¹, G. Y. Zhang¹⁹, H. Zhang⁶⁸, H. H. Zhang⁵⁶, H. H. Zhang³²,
H. Q. Zhang^{1,55,60}, H. Y. Zhang^{1,55}, J. J. Zhang⁴⁹, J. L. Zhang⁷⁴, J. Q. Zhang³⁹,
J. W. Zhang^{1,55,60}, J. X. Zhang^{36,j,k}, J. Y. Zhang¹, J. Z. Zhang^{1,60}, Jianyu Zhang^{1,60},
Jiawei Zhang^{1,60}, L. M. Zhang⁵⁸, L. Q. Zhang⁵⁶, Lei Zhang⁴⁰, P. Zhang¹,
Q. Y. Zhang^{37,78}, Shuihan Zhang^{1,60}, Shulei Zhang^{24,h}, X. D. Zhang⁴³, X. M. Zhang¹,
X. Y. Zhang⁴⁷, X. Y. Zhang⁵², Y. Zhang⁶⁶, Y. T. Zhang⁷⁸, Y. H. Zhang^{1,55},
Yan Zhang^{68,55}, Yao Zhang¹, Z. H. Zhang¹, Z. L. Zhang³², Z. Y. Zhang⁷³, Z. Y. Zhang⁴¹,
G. Zhao¹, J. Zhao³⁷, J. Y. Zhao^{1,60}, J. Z. Zhao^{1,55}, Lei Zhao^{68,55}, Ling Zhao¹,
M. G. Zhao⁴¹, S. J. Zhao⁷⁸, Y. B. Zhao^{1,55}, Y. X. Zhao^{29,60}, Z. G. Zhao^{68,55},
A. Zhemchugov^{34,a}, B. Zheng⁶⁹, J. P. Zheng^{1,55}, W. J. Zheng^{1,60}, Y. H. Zheng⁶⁰,
B. Zhong³⁹, X. Zhong⁵⁶, H. Zhou⁴⁷, L. P. Zhou^{1,60}, X. Zhou⁷³, X. K. Zhou⁶⁰,
X. R. Zhou^{68,55}, X. Y. Zhou³⁷, Y. Z. Zhou^{11,f}, J. Zhu⁴¹, K. Zhu¹, K. J. Zhu^{1,55,60},
L. Zhu³², L. X. Zhu⁶⁰, S. H. Zhu⁶⁷, S. Q. Zhu⁴⁰, T. J. Zhu^{11,f}, W. J. Zhu^{11,f},
Y. C. Zhu^{68,55}, Z. A. Zhu^{1,60}, J. H. Zou¹, J. Zu^{68,55}

(BESIII Collaboration)

¹ *Institute of High Energy Physics, Beijing 100049, People's Republic of China*

² *Beihang University, Beijing 100191, People's Republic of China*

³ *Beijing Institute of Petrochemical Technology, Beijing 102617, People's Republic of China*

⁴ *Bochum Ruhr-University, D-44780 Bochum, Germany*

⁵ *Carnegie Mellon University, Pittsburgh, Pennsylvania 15213, USA*

⁶ *Central China Normal University, Wuhan 430079, People's Republic of China*

⁷ *Central South University, Changsha 410083, People's Republic of China*

⁸ *China Center of Advanced Science and Technology, Beijing 100190, People's Republic of China*

⁹ *China University of Geosciences, Wuhan 430074, People's Republic of China*

¹⁰ *COMSATS University Islamabad, Lahore Campus, Defence Road, Off Raiwind Road, 54000 Lahore, Pakistan*

¹¹ *Fudan University, Shanghai 200433, People's Republic of China*

¹² *G.I. Budker Institute of Nuclear Physics SB RAS (BINP), Novosibirsk 630090, Russia*

¹³ *GSI Helmholtzcentre for Heavy Ion Research GmbH, D-64291 Darmstadt, Germany*

¹⁴ *Guangxi Normal University, Guilin 541004, People's Republic of China*

¹⁵ *Guangxi University, Nanning 530004, People's Republic of China*

¹⁶ *Hangzhou Normal University, Hangzhou 310036, People's Republic of China*

¹⁷ *Hebei University, Baoding 071002, People's Republic of China*

¹⁸ *Helmholtz Institute Mainz, Staudinger Weg 18, D-55099 Mainz, Germany*

¹⁹ *Henan Normal University, Xinxiang 453007, People's Republic of China*

²⁰ *Henan University of Science and Technology, Luoyang 471003, People's Republic of China*

²¹ *Henan University of Technology, Zhengzhou 450001, People's Republic of China*

²² *Huangshan College, Huangshan 245000, People's Republic of China*

²³ *Hunan Normal University, Changsha 410081, People's Republic of China*

- ²⁴ *Hunan University, Changsha 410082, People's Republic of China*
- ²⁵ *Indian Institute of Technology Madras, Chennai 600036, India*
- ²⁶ *Indiana University, Bloomington, Indiana 47405, USA*
- ²⁷ *INFN Laboratori Nazionali di Frascati, (A)INFN Laboratori Nazionali di Frascati, I-00044, Frascati, Italy; (B)INFN Sezione di Perugia, I-06100, Perugia, Italy; (C)University of Perugia, I-06100, Perugia, Italy*
- ²⁸ *INFN Sezione di Ferrara, (A)INFN Sezione di Ferrara, I-44122, Ferrara, Italy; (B)University of Ferrara, I-44122, Ferrara, Italy*
- ²⁹ *Institute of Modern Physics, Lanzhou 730000, People's Republic of China*
- ³⁰ *Institute of Physics and Technology, Peace Avenue 54B, Ulaanbaatar 13330, Mongolia*
- ³¹ *Instituto de Alta Investigación, Universidad de Tarapacá, Casilla 7D, Arica, Chile*
- ³² *Jilin University, Changchun 130012, People's Republic of China*
- ³³ *Johannes Gutenberg University of Mainz, Johann-Joachim-Becher-Weg 45, D-55099 Mainz, Germany*
- ³⁴ *Joint Institute for Nuclear Research, 141980 Dubna, Moscow region, Russia*
- ³⁵ *Justus-Liebig-Universitaet Giessen, II. Physikalisches Institut, Heinrich-Buff-Ring 16, D-35392 Giessen, Germany*
- ³⁶ *Lanzhou University, Lanzhou 730000, People's Republic of China*
- ³⁷ *Liaoning Normal University, Dalian 116029, People's Republic of China*
- ³⁸ *Liaoning University, Shenyang 110036, People's Republic of China*
- ³⁹ *Nanjing Normal University, Nanjing 210023, People's Republic of China*
- ⁴⁰ *Nanjing University, Nanjing 210093, People's Republic of China*
- ⁴¹ *Nankai University, Tianjin 300071, People's Republic of China*
- ⁴² *National Centre for Nuclear Research, Warsaw 02-093, Poland*
- ⁴³ *North China Electric Power University, Beijing 102206, People's Republic of China*
- ⁴⁴ *Peking University, Beijing 100871, People's Republic of China*
- ⁴⁵ *Qufu Normal University, Qufu 273165, People's Republic of China*
- ⁴⁶ *Shandong Normal University, Jinan 250014, People's Republic of China*
- ⁴⁷ *Shandong University, Jinan 250100, People's Republic of China*
- ⁴⁸ *Shanghai Jiao Tong University, Shanghai 200240, People's Republic of China*
- ⁴⁹ *Shanxi Normal University, Linfen 041004, People's Republic of China*
- ⁵⁰ *Shanxi University, Taiyuan 030006, People's Republic of China*
- ⁵¹ *Sichuan University, Chengdu 610064, People's Republic of China*
- ⁵² *Soochow University, Suzhou 215006, People's Republic of China*
- ⁵³ *South China Normal University, Guangzhou 510006, People's Republic of China*
- ⁵⁴ *Southeast University, Nanjing 211100, People's Republic of China*
- ⁵⁵ *State Key Laboratory of Particle Detection and Electronics, Beijing 100049, Hefei 230026, People's Republic of China*
- ⁵⁶ *Sun Yat-Sen University, Guangzhou 510275, People's Republic of China*
- ⁵⁷ *Suranaree University of Technology, University Avenue 111, Nakhon Ratchasima 30000, Thailand*
- ⁵⁸ *Tsinghua University, Beijing 100084, People's Republic of China*
- ⁵⁹ *Turkish Accelerator Center Particle Factory Group, (A)Istinye University, 34010,*

- Istanbul, Turkey; (B)Near East University, Nicosia, North Cyprus, Mersin 10, Turkey*
- ⁶⁰ *University of Chinese Academy of Sciences, Beijing 100049, People's Republic of China*
- ⁶¹ *University of Groningen, NL-9747 AA Groningen, The Netherlands*
- ⁶² *University of Hawaii, Honolulu, Hawaii 96822, USA*
- ⁶³ *University of Jinan, Jinan 250022, People's Republic of China*
- ⁶⁴ *University of Manchester, Oxford Road, Manchester, M13 9PL, United Kingdom*
- ⁶⁵ *University of Muenster, Wilhelm-Klemm-Strasse 9, 48149 Muenster, Germany*
- ⁶⁶ *University of Oxford, Keble Road, Oxford OX13RH, United Kingdom*
- ⁶⁷ *University of Science and Technology Liaoning, Anshan 114051, People's Republic of China*
- ⁶⁸ *University of Science and Technology of China, Hefei 230026, People's Republic of China*
- ⁶⁹ *University of South China, Hengyang 421001, People's Republic of China*
- ⁷⁰ *University of the Punjab, Lahore-54590, Pakistan*
- ⁷¹ *University of Turin and INFN, (A)University of Turin, I-10125, Turin, Italy; (B)University of Eastern Piedmont, I-15121, Alessandria, Italy; (C)INFN, I-10125, Turin, Italy*
- ⁷² *Uppsala University, Box 516, SE-75120 Uppsala, Sweden*
- ⁷³ *Wuhan University, Wuhan 430072, People's Republic of China*
- ⁷⁴ *Xinyang Normal University, Xinyang 464000, People's Republic of China*
- ⁷⁵ *Yantai University, Yantai 264005, People's Republic of China*
- ⁷⁶ *Yunnan University, Kunming 650500, People's Republic of China*
- ⁷⁷ *Zhejiang University, Hangzhou 310027, People's Republic of China*
- ⁷⁸ *Zhengzhou University, Zhengzhou 450001, People's Republic of China*
- ^a *Also at the Moscow Institute of Physics and Technology, Moscow 141700, Russia*
- ^b *Also at the Novosibirsk State University, Novosibirsk, 630090, Russia*
- ^c *Also at the NRC "Kurchatov Institute", PNPI, 188300, Gatchina, Russia*
- ^d *Also at Goethe University Frankfurt, 60323 Frankfurt am Main, Germany*
- ^e *Also at Key Laboratory for Particle Physics, Astrophysics and Cosmology, Ministry of Education; Shanghai Key Laboratory for Particle Physics and Cosmology; Institute of Nuclear and Particle Physics, Shanghai 200240, People's Republic of China*
- ^f *Also at Key Laboratory of Nuclear Physics and Ion-beam Application (MOE) and Institute of Modern Physics, Fudan University, Shanghai 200443, People's Republic of China*
- ^g *Also at State Key Laboratory of Nuclear Physics and Technology, Peking University, Beijing 100871, People's Republic of China*
- ^h *Also at School of Physics and Electronics, Hunan University, Changsha 410082, China*
- ⁱ *Also at Guangdong Provincial Key Laboratory of Nuclear Science, Institute of Quantum Matter, South China Normal University, Guangzhou 510006, China*
- ^j *Also at Frontiers Science Center for Rare Isotopes, Lanzhou University, Lanzhou 730000, People's Republic of China*
- ^k *Also at Lanzhou Center for Theoretical Physics, Lanzhou University, Lanzhou 730000,*

People's Republic of China

^l *Also at the Department of Mathematical Sciences, IBA, Karachi , Pakistan*

1 Introduction

The phenomenon of CP violation in the standard model (SM) is parametrized by a single irreducible phase in the complex Cabibbo-Kobayashi-Maskawa (CKM) quark-mixing matrix [1, 2], which describes the weak interaction of quarks. Exploiting the unitary nature of the CKM matrix, this CP -violating phase can be represented on the complex plane as the argument of a particular combination of the CKM elements $V_{qq'}$. The phase $-\arg[(V_{ub}^*V_{us})/(V_{cb}^*V_{cs})]$ is denoted by γ and can be measured by studying interference between decays with identical final states where one proceeds via a $b \rightarrow u$ transition [3–5]. The decay $B^\pm \rightarrow Dh^\pm$, where h^\pm denotes a K^\pm or π^\pm and D a superposition of the flavor states of neutral D meson, proceeds almost purely at tree-level; electroweak box and loop corrections are below $\mathcal{O}(10^{-7})$ [6], thereby excluding the possibility of loop-level contributions from beyond-the-SM physics [7]. The absence of theoretical uncertainties makes this channel ideal to determine γ . The γ determination method put forward in Refs. [8, 9] requires the D meson to decay into self-conjugate multi-body final states such as $K_S^0\pi^+\pi^-$. Such multi-body D -meson decays provide regions of phase space where interference between CP -eigenstates of the D meson [3], and Cabibbo-favoured (CF) and doubly Cabibbo-suppressed (DCS) [4] decays take place, which allows γ and the strong-dynamics of the B decay to be extracted from a single decay mode.

Although the current world average of γ is still statistically limited, the statistical uncertainty has reduced by approximately a factor eight over the last decade, and the ultimate data samples of LHCb and Belle II should result in a statistical uncertainty in γ close to 1° . The primary source of systematic uncertainty is inputs from the D -decay parameters [10, 11]. These inputs are the strong-phase differences $\Delta\delta_D$, between D^0 and \bar{D}^0 decays which are measured in quantum-correlated D decay [12, 13]. The strong-phase difference arising from the interference of D^0 and \bar{D}^0 decaying into a common final state $K_S^0\pi^+\pi^-$ is a critical input not only to the γ measurement using $B^\pm \rightarrow DK^\pm$ decay channels but also to other important flavor studies: the time-dependent measurement of the CKM angle β through $B^0 \rightarrow \bar{D}^{(*)0}h^0$ decays [14, 15] and the measurement of CP violation and mixing in neutral D meson system [16].

Quantum-correlated $D\bar{D}$ events at $\psi(3770)$ recorded at BESIII give access to the strong-phase difference when D decays are reconstructed by means of flavor tagging [17]. The pairs of D mesons are quantum-correlated because they are produced in a $J^{PC} = 1^{--}$ state with an anti-symmetric wavefunction,

$$|\psi(3770)\rangle = |D\bar{D}\rangle = \frac{1}{\sqrt{2}} (|D^0\rangle|\bar{D}^0\rangle - |\bar{D}^0\rangle|D^0\rangle), \quad (1.1)$$

which constrains the decay product of one D meson given the other, discussed more specifically in section 2. A model-independent BESIII analysis measured the average sine and cosine of $\Delta\delta_D$ for $K_S^0\pi^+\pi^-$ (c_i, s_i) and $K_L^0\pi^+\pi^-$ (c'_i, s'_i) [18, 19]. Inclusion of the $K_L^0\pi^+\pi^-$ mode provides a three-times-larger data sample at BESIII due to higher K_L^0 reconstruction efficiency and combinatorics of $D\bar{D} \rightarrow (K_S^0\pi^+\pi^-)^2$ versus $D\bar{D} \rightarrow (K_S^0\pi^+\pi^-, K_L^0\pi^+\pi^-)$ decays. However, including these $K_L^0\pi^+\pi^-$ decays introduces a systematic uncertainty related

to assumptions about the values of complex *U-spin breaking* parameters ($\hat{\rho}$) that separate the decay amplitudes of $D^0 \rightarrow K_L^0 \pi^+ \pi^-$ and $D^0 \rightarrow K_S^0 \pi^+ \pi^-$ modes. In previous analyses [18–20], the nominal value of the parameters was unity; and a systematic uncertainty on this assumption was derived by assuming $|\hat{\rho}|$ had an uncertainty of 50% and $\arg(\hat{\rho})$ could have any value in the interval $(-180^\circ, 180^\circ)$. These U-spin breaking parameters, which are discussed in greater detail in section 2, have never been experimentally determined and the only way to measure them is through an amplitude analysis of the $D^0 \rightarrow K_L^0 \pi^+ \pi^-$ decay. This paper presents the first experimental measurements of $\hat{\rho}$ in this decay.

The remainder of this paper is organized as follows. A brief discussion about the model-independent measurement of strong-phase parameters and a review of amplitude parametrizations for a three-body decay are given in section 2. An overview of the BESIII detector and the simulations performed for this analysis is given in section 3, while section 4 lists various event selection criteria adopted to select the data samples. The amplitude analysis implementation and validation are presented in section 5. Results are given in section 6, while section 7 presents a study of systematic uncertainties. Section 8 provides additional model predictions in the form of *CP* content of $K_S^0 \pi^+ \pi^-$ and $K_L^0 \pi^+ \pi^-$ modes and the ratio of their branching fractions in *D* decays. Section 9 reports the conclusions.

2 Strong-phase and amplitude-analysis formalism

In this section we first define the strong-phase parameters and how those for $D \rightarrow K_S^0 \pi^+ \pi^-$ and $D \rightarrow K_L^0 \pi^+ \pi^-$ are related together. Then we discuss the amplitude-analysis technique employed to determine the $\hat{\rho}$ parameters.

The *D*-decay parameters that appear in these studies are cosines and sines of the strong-phase difference averaged over regions of phase space. The two-dimensional phase space of $K_S^0 \pi^+ \pi^-$ and $K_L^0 \pi^+ \pi^-$ decay modes is described in terms of pairwise invariant masses of the final-state particles. Of the three possible permutations, only two will be independent, forming a Dalitz plot (DP) for which the phase space is uniform within its boundaries. In this paper we use invariant squared masses of $K_{S(L)}^0 \pi^+$ and $K_{S(L)}^0 \pi^-$, which are written as $s_{K_{S(L)}^0 \pi^+}$ and $s_{K_{S(L)}^0 \pi^-}$, respectively. The DP is divided into bins to gain sensitivity to the large variations in the strong-phase difference $\Delta\delta_D$ across the DP. One common binning scheme is the *equal- $\Delta\delta_D$* binning that minimizes the variation in the values of $\Delta\delta_D$ in each bin; this scheme is shown in figure 1. The DP is divided into sixteen bins, which are symmetric about the line $s_{K_{S(L)}^0 \pi^+} = s_{K_{S(L)}^0 \pi^-}$. The weighted averages of cosines and sines of the strong-phase difference in the i^{th} bin of the DP are given by

$$c_i = \frac{1}{\sqrt{\int_i |A_D(\mathbf{x})|^2 d\mathbf{x} \int_i |A_{\bar{D}}(\mathbf{x})|^2 d\mathbf{x}}} \int_i |A_D(\mathbf{x})| |A_{\bar{D}}(\mathbf{x})| \cos(\Delta\delta_D) d\mathbf{x}, \quad (2.1)$$

and an analogous expression with sine of the strong-phase difference, where $A_D(\mathbf{x})$ and $A_{\bar{D}}(\mathbf{x})$ are the decay amplitudes of D^0 and \bar{D}^0 , respectively, at point $\mathbf{x} = (s_{K_S^0 \pi^+}, s_{K_S^0 \pi^-})$ in the same bin on the DP of the final state $K_S^0 \pi^+ \pi^-$. A similar definition of strong-phase parameters c'_i and s'_i can be written for the $K_L^0 \pi^+ \pi^-$ decay mode. The primed parameters henceforth correspond to the $K_L^0 \pi^+ \pi^-$ mode.

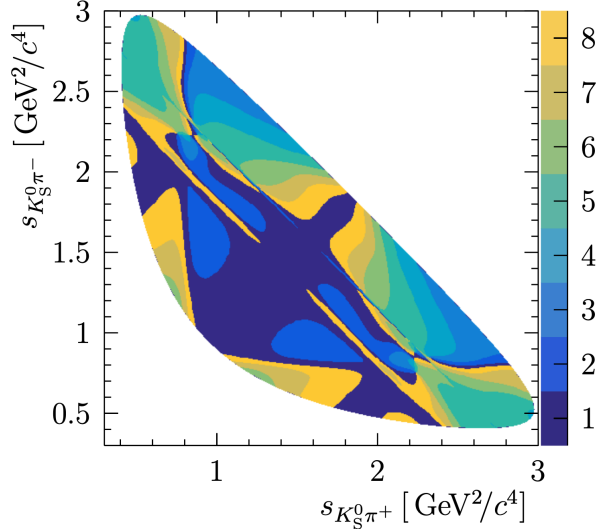


Figure 1: Equal- $\Delta\delta_D$ bins on the Dalitz plot of $D^0 \rightarrow K_S^0 \pi^+ \pi^-$ decay.

In a model-independent measurement of $c_i^{(j)}$ and $s_i^{(j)}$ with quantum-correlated $D\bar{D}$ events, the observables are yields of events for which the decays of both the D meson states are reconstructed, known as *double-tagged* (DT) yields. More precisely, the first set of observables are the expected yields of $K_S^0 \pi^+ \pi^-$ or $K_L^0 \pi^+ \pi^-$ in the i^{th} DP bin that are reconstructed against an exact or approximate CP eigenstate such as $K^+ K^-$ or $\pi^+ \pi^- \pi^0$. These observables, conventionally denoted by $M_i^{(j)}$ for the $K_{S(L)}^0 \pi^+ \pi^-$ mode, are only sensitive to $c_i^{(j)}$ but not $s_i^{(j)}$. The second set of observables are yields of the signal $K_{S(L)}^0 \pi^+ \pi^-$ mode in the i^{th} DP bin reconstructed against another $K_S^0 \pi^+ \pi^-$ mode in the j^{th} bin of its DP. These are denoted by $M_{ij}^{(j)}$ and are sensitive to both $c_i^{(j)}$ and $s_i^{(j)}$. Furthermore, the measured parameter differences between $K_S^0 \pi^+ \pi^-$ and $K_L^0 \pi^+ \pi^-$ modes, $\Delta c_i^{\text{meas}} = (c_i - c_i')$ and $\Delta s_i^{\text{meas}} = (s_i - s_i')$ are constrained to their model-predicted values Δc_i^{pred} and Δs_i^{pred} , respectively. The constraint is implemented via a χ^2 penalty term:

$$\chi^2 = \sum_i \left[\left(\Delta c_i^{\text{meas}} - \Delta c_i^{\text{pred}} \right) / \delta(\Delta c_i^{\text{pred}}) \right]^2 + \sum_i \left[\left(\Delta s_i^{\text{meas}} - \Delta s_i^{\text{pred}} \right) / \delta(\Delta s_i^{\text{pred}}) \right]^2, \quad (2.2)$$

where $\delta(\Delta c_i^{\text{pred}})$ and $\delta(\Delta s_i^{\text{pred}})$ are the associated uncertainties on the model-predicted differences. Including the $K_L^0 \pi^+ \pi^-$ final state improves sensitivity, particularly to $s_i^{(j)}$.

The uncertainties on the model-predicted values of the differences, $\delta(\Delta c_i^{\text{pred}})$ and $\delta(\Delta s_i^{\text{pred}})$ are dominated by assumptions associated with the U-spin breaking parameters [18, 19]. This uncertainty motivates an amplitude analysis of $D^0 \rightarrow K_L^0 \pi^+ \pi^-$, which will test these assumptions and determine a well defined data-driven uncertainty.

With the motivation for an amplitude analysis of $D^0 \rightarrow K_L^0 \pi^+ \pi^-$ described, we now provide the formalism for such an analysis. Any three-body decay $D \rightarrow abc$ can proceed via multiple quasi-independent two-body intermediate channels:

$$D \rightarrow rc, \quad r \rightarrow ab, \quad (2.3)$$

where r is an intermediate resonance. The total effective amplitude of this decay topology is given by a coherent sum of all the contributing resonant channels. This approximation is called the *isobar model*, where the contributing intermediate amplitudes are referred to as the *isobars*. Isobars can be modeled with various complex dynamical functions, the choice of which depends on the spin and width of the resonance. In addition to the resonant modes, the total decay amplitude may also include a three-body *non-resonant* channel:

$$\mathcal{A}(\mathbf{x}) = \mathcal{A}_{\text{resonant}} + \mathcal{A}_{\text{NR}} = \sum_r a_r e^{i\phi_r} A_r(\mathbf{x}) + a_0 e^{i\phi_0}, \quad (2.4)$$

where $\mathcal{A}(\mathbf{x})$ is the final decay amplitude at position \mathbf{x} in the DP. Here the complex coupling parameters $a_r e^{i\phi_r}$ correspond to resonant contributions denoted by r and provide relative magnitudes and phases to each of these resonant amplitudes. As the DP phase space is uniform, only the dynamical part $A_r(\mathbf{x})$ of the total decay rate results in variations of event density over the DP. Nominally, the dynamics of the modes associated with well isolated and narrow resonant structures with spin one or two are described by relativistic *Breit-Wigner* functions. In contrast, dynamics of broad overlapping resonant structures, which usually is the case with scalars, are parametrized using the K-matrix formulation borrowed from scattering theory. For the subsequent discussions on various parametrizations in the rest of this section, a generic decay chain will be referred to, as in eq. 2.3, with an angular-momentum transfer $J_D \rightarrow j_r + L$, where J_D and j_r denote the intrinsic spins of D and r , and L is the relative orbital angular momentum between r and c .

Relativistic *Breit-Wigner* functions are phenomenological descriptions of non-overlapping intermediate transitions that are away from threshold. Their dynamical structure takes the form

$$T_r(s) = \frac{1}{m_0^2 - s - im_0\Gamma(s)}, \quad (2.5)$$

where m_0 is the resonance mass and \sqrt{s} is the resonance two-particle invariant mass. The momentum-dependent resonance width $\Gamma(s)$ relates to the pole width (Γ_0) as

$$\Gamma(s) = \Gamma_0 \frac{m_0}{\sqrt{s}} \left(\frac{q}{q_0} \right)^{(2L+1)} \mathcal{B}_r^L(q, q_0). \quad (2.6)$$

Pole masses and widths in this analysis are fixed to the PDG values [21]. The function $\mathcal{B}_r^L(q, q_0)$ is the centrifugal-barrier factor [22] in the decay $r \rightarrow ab$, where q is the momentum transfer in the r decay in its rest frame and q_0 is q evaluated at m_0 . The full Breit-Wigner amplitude description includes, in addition to the dynamical part $T_r(s)$, barrier factors corresponding to P - and D -wave decays of the initial state D meson and resonance r decays, \mathcal{B}_D^L and \mathcal{B}_r^L respectively, and an explicit spin-dependent factor (\mathcal{Z}_L):

$$A_r^{BW} = T_r(s) \times \mathcal{B}_r^L(q, q_0) \times \mathcal{B}_D^L(p, p_0) \times \mathcal{Z}_L(J_D, j_r, \mathbf{p}, \mathbf{q}). \quad (2.7)$$

Here p denotes momentum of the spectator particle c in the resonance rest frame and p_0 is the corresponding on-shell value. Scaling of the Breit-Wigner lineshape by the barrier factors optimizes the enhancement or dampening of the total amplitude depending upon the relative orbital angular momentum (or the spin of the resonance) of the decay and the

L	Form factor $\mathcal{B}_r^L(q, q_0)$
0	1
1	$\sqrt{\frac{1+q_0^2 d^2}{1+q^2 d^2}}$
2	$\sqrt{\frac{9+3q_0^2 d^2+(q_0^2 d^2)^2}{9+3q^2 d^2+(q^2 d^2)^2}}$

Table 1: Normalized Blatt-Weisskopf barrier factors [23] for resonance decay exhibiting spin and momentum-dependent effects.

linear momenta of the particles involved. For resonances with spin greater than or equal to one and small decay interaction radius (or impact parameter) of the order 1 fm, large momentum transfer in the a, b system is disfavoured because of limited orbital angular momentum between r and c . *Blatt-Weisskopf* form factors [23], normalized to unity at $q = q_0$, are used to parametrize the barrier factors whose functional forms are given in table 1, where d denotes the interaction radius of the parent particle. Similar expressions for D -decay barrier factors can be written in terms of momentum of the spectator particle evaluated in the D rest frame.

The spin-dependence of the decay amplitudes are derived using covariant spin-tensor or Rarita-Schwinger formalism [24–27]. The pure spin-tensors for spin 1 and 2 from spin-projection operators Θ and the break-up four-momentum $k^\mu = a^\mu - b^\mu$ in the resonance rest frame (so that three-momentum $\mathbf{k} = 2\mathbf{q}$) are given by

$$S_\mu = \Theta_{\mu\nu} k^\nu, \quad (2.8)$$

$$T_{\mu\nu} = \Theta_{\mu\nu\rho\sigma} k^\rho k^\sigma. \quad (2.9)$$

Using the above defined spin-tensors together with the orthogonality and spacelike conditions on Lorentz invariant functions of rank one and two for P and D wave, respectively, when summed over all the polarization states, it is possible to arrive at the following definitions of the angular decay amplitude:

$$A(0 \rightarrow 1 + 1) : \mathcal{Z}_{L=1} = \Theta^{\mu\nu} S_\mu \mathcal{L}_\nu, \quad (2.10)$$

$$A(0 \rightarrow 2 + 2) : \mathcal{Z}_{L=2} = \Theta^{\mu\rho} \Theta^{\nu\sigma} T_{\mu\nu} \mathcal{M}_{\rho\sigma}, \quad (2.11)$$

where \mathcal{L} and \mathcal{M} are normalized tensors describing the states of relative orbital angular momenta $L = 1$ and $L = 2$. Simplified expressions for the angular amplitudes in terms of four-momenta of the states involved and their invariant masses are given in appendix A.

Overlapping S -wave pole production with multiple channels in two-body scattering processes are best described by the K -matrix formulation [28–30]. A sum of Breit-Wigner functions to describe such broad resonant structures violate the unitarity of the transition matrix \mathcal{T} . The idea is to write the total effective \mathcal{T} matrix in terms of the K matrix

$$\hat{\mathcal{T}} = (1 - i\hat{K}\omega)^{-1}\hat{K}. \quad (2.12)$$

The K -matrix contains contributions from all the poles, intermediate channels and all possible couplings. Here the parameter ω is a diagonal matrix with the phase-space densities of various channels involved as its elements. As an example, in low energy $\pi\pi \rightarrow \pi\pi$ scattering, the total amplitude carries a contribution from coupling between the resonance $f_0(980)$ and a KK channel, which is partly responsible for the sharp dip observed in the scattering amplitude near 1 GeV. A simple Breit-Wigner function cannot explain this variation in the amplitude.

This recipe can be translated to decay processes involving broad overlapping resonance structures produced in an S -wave. An initial state first couples to K -matrix poles with strength parametrized by β_α for pole α , and these poles in turn couple to various intermediate channels i in the K -matrix with strengths characterized by g_i^α . Direct coupling between initial state and these K -matrix channels is also a possibility and the corresponding strength is denoted by f_{1i}^{prod} , scaling a slowly varying polynomial term in s and an arbitrary parameter s_0^{prod} , which are fixed from a global analysis of $\pi\pi$ scattering data [29]. Summing these contributions together results in the *production vector* \hat{P} :

$$\hat{P}_i = \sum_{\alpha} \frac{\beta_{\alpha} g_i^{\alpha}}{m_{\alpha}^2 - s} + f_{1i}^{\text{prod}} \frac{1 - s_0^{\text{prod}}}{s - s_0^{\text{prod}}}, \quad (2.13)$$

where m_{α} are the pole masses and s is the kinematic variable, in this case the invariant squared-mass of the two pions from the three-body decay. The structure of the K matrix in a decay process with poles α and decay channels denoted by i and j is given by

$$K_{ij}(s) = \left(\sum_{\alpha} \frac{g_i^{\alpha} g_j^{\alpha}}{m_{\alpha}^2 - s} + f_{ij}^{\text{scatt}} \frac{1 - s_0^{\text{scatt}}}{s - s_0^{\text{scatt}}} \right) f_{A0}(s). \quad (2.14)$$

The intermediate channels considered in the present case are $\pi\pi$, KK , $\pi\pi\pi\pi$, $\eta\eta$ and $\eta\eta'$. In addition to the pole terms, direct scatterings between channels are also considered with strengths f_{ij}^{scatt} in a polynomial term in s and parameter s_0^{scatt} [29]. An arbitrary kinematic singularity appears below the $\pi\pi$ production threshold at $\sqrt{s} \sim m_{\pi}/\sqrt{2}$. The so-called *Adler-zero* term, $f_{A0}(s)$ [15] is multiplied to the entire K -matrix to suppress it. Finally, the total production amplitude for a final decay channel j can be written in terms of the P vector as

$$A_{\pi\pi}^{(L=0)}(s)_j = \left(I - i\hat{K}(s)\hat{\omega}(s) \right)_{ji}^{-1} P_i(s). \quad (2.15)$$

In the present case of $D^0 \rightarrow K^0(\pi\pi)_S$, five poles of K matrix are considered, which are summarized in table 2. These may be associated with \mathcal{T} poles as physical resonances: $f_0(980)$, $f_0(1370)$, $f_0(1500)$, $f_0(1710)$, and a broad spectrum $f_0(1200 - 1600)$. Moreover, K matrix couplings associated with only $\pi\pi$ final states, *i.e.*, $j = 1$ or first row of the $(I - i\hat{K}\hat{\omega})^{-1}$ matrix, are considered.

The $K\pi$ scalar contribution is described by a parametrization developed by the LASS collaboration, again originally designed for scattering processes [31]. The first scalar excitation of the $K\pi$ state is $K_0^*(1430)$, so the CF non-resonant process carries a considerably larger contribution and is described by the empirical LASS formulation. The total LASS

α	m_α [GeV/ c^2]
1	0.65100
2	1.20360
3	1.55817
4	1.21000
5	1.82206

Table 2: Poles and couplings in K -matrix [15, 29]. The intermediate channels include $\pi\pi$, KK , $\pi\pi\pi\pi$, $\eta\eta$ and $\eta\eta'$

amplitude is a sum of a Breit-Wigner resonant term and a non-resonant scattering term, scaled by an overall complex coupling parameter as

$$A_{K\pi}^{(L=0)}(s) = a_r e^{i\phi_r} (R \sin \delta_R e^{i\delta_R} e^{i2\delta_S} + S \sin \delta_S e^{i\delta_S}), \quad (2.16)$$

where

$$\delta_R = \phi_R + \tan^{-1} \left[\frac{m_0 \Gamma(s)}{m_0^2 - s} \right],$$

$$\delta_S = \phi_S + \cot^{-1} \left[\frac{1}{aq} + \frac{r_{\text{int}} q}{2} \right].$$

The parameters $R e^{i\phi_R}$ and $S e^{i\phi_S}$ are relative complex amplitudes of the resonant and non-resonant (direct scattering) terms, respectively. The parameter a is the scattering length and r_{int} is the effective interaction length in the case of direct scattering. More details can be found in Ref. [31]. The same parametrization is used for the DCS $K_0^*(1430)^+$ resonant process for which a_r and ϕ_r are again nominally to be determined from the fit.

In the remainder of this section we discuss the application of the isobar model to $D^0 \rightarrow K_{S,L}^0 \pi^+ \pi^-$ decays. Non-trivial effects on the rate of hadronic decays involving pions and neutral kaons as a result of DCS transitions interfering with CF transitions are expected [32]. A manifestation of this interference effect is a small difference in the

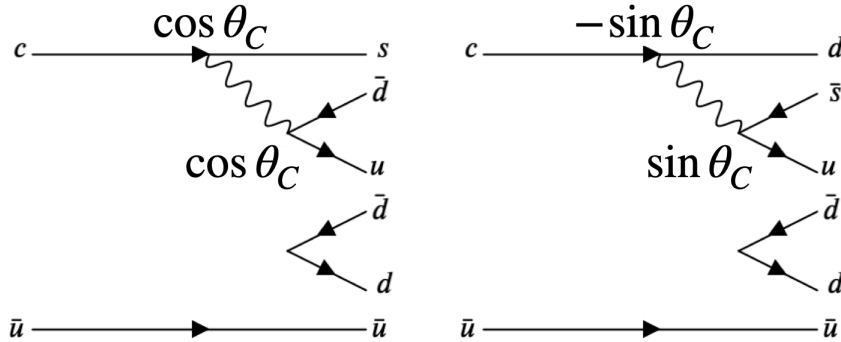


Figure 2: CF $D^0 \rightarrow \bar{K}^0 \pi^+ \pi^-$ (left) and DCS $D^0 \rightarrow K^0 \pi^+ \pi^-$ (right) decay diagrams.

decay rates of processes involving a K_S^0 versus a K_L^0 in the final state. Consider the decay process $D^0 \rightarrow K_S^0 \pi^+ \pi^-$, which can proceed both via the CF $D^0 \rightarrow \bar{K}^0 \pi^+ \pi^-$ and the DCS $D^0 \rightarrow K^0 \pi^+ \pi^-$.

In addition to the pure CF and DCS sub-transitions, as shown in figure 2, a mixture of these, where the two pions are produced in a CP eigenstate resonance, is also a viable transition process to the $K_S^0 \pi^+ \pi^-$ final state. Note that the two amplitudes would be identical under the interchange of the s and d quarks involved in the weak interaction, which is referred to as U-spin symmetry. Using the phase convention $CP|K^0\rangle = -|\bar{K}^0\rangle$, the partial amplitude of intermediate processes involving only neutral CP eigenstate resonances k_{CP} , *i.e.* $D^0 \rightarrow K_S^0(\pi^+ \pi^-)_{k_{CP}}$, can be written as a superposition of $D^0 \rightarrow \bar{K}^0 \pi^+ \pi^-$ and $D^0 \rightarrow K^0 \pi^+ \pi^-$ as follows

$$A(D^0 \rightarrow K_S^0(\pi\pi)_{k_{CP}}) = \frac{1}{\sqrt{2}} (A(D^0 \rightarrow \bar{K}^0(\pi^+ \pi^-)) - A(D^0 \rightarrow K^0(\pi^+ \pi^-))) \quad (2.17a)$$

$$= \frac{1}{\sqrt{2}} A(D^0 \rightarrow \bar{K}^0(\pi^+ \pi^-)) \left(1 - \frac{A(D^0 \rightarrow K^0(\pi^+ \pi^-))}{A(D^0 \rightarrow \bar{K}^0(\pi^+ \pi^-))} \right). \quad (2.17b)$$

Defining $A(D^0 \rightarrow K^0(\pi^+ \pi^-))/A(D^0 \rightarrow \bar{K}^0(\pi^+ \pi^-)) = -\tan^2 \theta_C \hat{\rho}$, where $\hat{\rho}$ may be understood as a *U-spin breaking* parameter, the $K_S^0 \pi^+ \pi^-$ CP transition amplitude can be written as

$$A(D^0 \rightarrow K_S^0(\pi\pi)_{k_{CP}}) = \frac{1}{\sqrt{2}} A(D^0 \rightarrow \bar{K}^0(\pi^+ \pi^-)) (1 + \hat{\rho}_{k_{CP}} \tan^2 \theta_C). \quad (2.17c)$$

The U-spin breaking parameter, $\hat{\rho} (= r e^{i\delta})$ is a complex and purely empirical quantity. For a three-body decay with multiple exclusive CP eigenstate resonant contributions (k_{CP}), $\hat{\rho}$ factors for each are denoted by $\hat{\rho}_{k_{CP}}$. The $\hat{\rho}$ parameters carry the phase-shifts generated as a result of DCS interference and naively, the magnitudes $|\rho|$ are expected to be $\sim \mathcal{O}(1)$ in the absence of any interference between CF and DCS transitions. However, the magnitudes should be empirically measured to consider the possibility of deviation from the nominal $\tan^2 \theta_C$ Cabibbo factor. A similar treatment for the decay process $D^0 \rightarrow K_L^0 \pi^+ \pi^-$ yields

$$A(D^0 \rightarrow K_L^0(\pi\pi)_{k_{CP}}) = \frac{1}{\sqrt{2}} A(D^0 \rightarrow \bar{K}^0(\pi^+ \pi^-)) (1 - \hat{\rho}_{k_{CP}} \tan^2 \theta_C). \quad (2.18a)$$

It is then straightforward to show that the CP -resonant amplitudes of $D^0 \rightarrow K_L^0 \pi^+ \pi^-$ decay process can be related to the $D^0 \rightarrow K_S^0(\pi^+ \pi^-)_{k_{CP}}$ amplitudes as

$$\frac{A(D^0 \rightarrow K_L^0(\pi\pi)_{k_{CP}})}{A(D^0 \rightarrow K_S^0(\pi\pi)_{k_{CP}})} = \frac{1 - \tan^2 \theta_C \hat{\rho}_{k_{CP}}}{1 + \tan^2 \theta_C \hat{\rho}_{k_{CP}}} \approx 1 - 2 \tan^2 \theta_C \hat{\rho}_{k_{CP}} + \mathcal{O}(\tan^4 \theta_C),$$

which results in the relation

$$A(D^0 \rightarrow K_L^0(\pi\pi)_{k_{CP}}) = (1 - 2 \tan^2 \theta_C \hat{\rho}_{k_{CP}}) \times A(D^0 \rightarrow K_S^0(\pi\pi)_{k_{CP}}), \quad (2.19)$$

where terms higher than second order in $\tan \theta_C$ are neglected. An amplitude model description of the $D^0 \rightarrow K_L^0 \pi^+ \pi^-$ decay mode is required for a constrained strong-phase measurement. The $K_L^0 \pi^+ \pi^-$ amplitude model can be obtained via the DCS interference motivated

modifications to the well studied $K_S^0\pi^+\pi^-$ model, such as the one stated in eq. 2.19. Another departure is expected in the DCS resonant modes such as $D^0 \rightarrow (K_{L,S}^0\pi^+)_{K^*\pi^-}$, with a relative minus sign between $K_S^0\pi^+\pi^-$ and $K_L^0\pi^+\pi^-$ amplitudes, again because of the phase structure in the definition of $K_{L,S}^0\pi^+\pi^-$ in terms of the flavor states. We insert this minus sign in the DCS amplitudes of $K_L^0\pi^+\pi^-$ instead of $K_S^0\pi^+\pi^-$ to maintain consistency with the standalone $K_S^0\pi^+\pi^-$ amplitude model that has no minus sign in the DCS parts. Doing so merely introduces an extra 180° phase added to the nominal DCS phases and does not affect any physics. The total amplitudes are

$$A(D^0 \rightarrow K_S^0\pi^+\pi^-) = \sum_r A_{K^0\pi\pi}^{CF} + \sum_{r'} A_{K^0\pi\pi}^{DCS} + \sum_{k_{CP}} A_{K_S^0(\pi^+\pi^-)_{k_{CP}}}^{CP}, \quad (2.20)$$

$$A(D^0 \rightarrow K_L^0\pi^+\pi^-) = \sum_r A_{K^0\pi\pi}^{CF} - \sum_{r'} A_{K^0\pi\pi}^{DCS} + \sum_{k_{CP}} (1 - 2\tan^2\theta_C \hat{\rho}_{k_{CP}}) A_{K_S^0(\pi^+\pi^-)_{k_{CP}}}^{CP}. \quad (2.21)$$

The only way to determine the $\hat{\rho}$ parameters associated with each of the two-body intermediate resonant structure contributions in $K_{S,L}^0\pi^+\pi^-$ decay process, is to fit an amplitude model for $D^0 \rightarrow K_L^0\pi^+\pi^-$, where the $D^0 \rightarrow K_S^0\pi^+\pi^-$ decay may be used as a constraint in a simultaneous fit.

3 BESIII detector and simulated sample

The BESIII detector [17] records symmetric e^+e^- collisions provided by the BEPCII storage ring [33], which operates with a peak luminosity of $1 \times 10^{33} \text{ cm}^{-2}\text{s}^{-1}$ in the center-of-mass energy range from 2.0 to 4.99 GeV. BESIII has collected large data samples in this energy region [34]. The cylindrical core of the BESIII detector covers 93% of the full solid angle and consists of a helium-based multilayer drift chamber (MDC), a plastic scintillator time-of-flight system (TOF), and a CsI(Tl) electromagnetic calorimeter (EMC), which are all enclosed in a superconducting solenoidal magnet providing a 1.0 T magnetic field. The solenoid is supported by an octagonal flux-return yoke with resistive plate counter muon identification modules interleaved with steel. The charged-particle momentum resolution at 1 GeV/ c is 0.5%, and the dE/dx resolution is 6% for electrons from Bhabha scattering. The EMC measures photon energies with a resolution of 2.5% (5%) at 1 GeV in the barrel (end cap) region. The time resolution in the TOF barrel region is 68 ps, while that in the end cap region is 110 ps.

The experimental data used were collected with a centre-of-mass energy corresponding the mass of the $\psi(3770)$ resonance. The sample size corresponds to an integrated luminosity of 2.93 fb^{-1} .

We also use simulated events to optimize our selection, identify background contributions and validate the amplitude analysis. In the BESIII software framework, starting from e^+e^- annihilation upto the charmonium resonance production part of the processes, including the initial-state radiation (ISR) effects and the beam energy spread of 0.97 MeV, are

simulated using the KKMC generator [35] and for the resonance decay, elaborate BESEVT-GEN models [36] are used for they also contain dynamical information of the decay. The resonances supported by KKMC include J/ψ , $\psi(2S)$, $\psi(3770)$, $\psi(4040)$, $\psi(4160)$, $\psi(4415)$ and other low lying resonances like ρ , ϕ , ω and their excitations.

Both inclusive and signal samples of simulated events are produced using the above mentioned generator packages, as well as a GEANT4 [37] - based detector geometry and response simulation package. The inclusive simulation sample in this analysis is prepared by adding together various simulated physics processes in proportion to their branching ratios. These physics processes include $D^0\bar{D}^0$ and D^+D^- from $\psi(3770)$, J/ψ and $\psi(2S)$ charmonium production along with ISR, lepton pair production and $q\bar{q}$ continuum. The size of the inclusive simulation sample used for background estimation is roughly ten times that of the experimental data. Simulated samples of $K_S^0\pi^+\pi^-$ and $K_L^0\pi^+\pi^-$ decays, with a size one hundred times that of experimental data, are produced to normalize the probability density in the amplitude fit. Simulated signal decays including resonant structures are produced to validate the amplitude fit.

4 Event selection

We use a sample of quantum-correlated $e^+e^- \rightarrow D^0\bar{D}^0$ events, which are produced close to the kinematic threshold for this process. No other particles accompany the D mesons, which results in a low-background environment to reconstruct the D candidates. We identify the flavor of the neutral D meson decaying into the signal modes $K_{S,L}^0\pi^+\pi^-$ by reconstructing the other D meson state in a flavor-specific mode, which is also commonly known as the *tag mode*, and this full-reconstruction technique is referred to as the *double-tag method*. The $K_L^0\pi^+\pi^-$ signal mode is reconstructed with the K_L^0 candidate treated as a *missing particle*, which makes using the semi-leptonic exact flavor-tag modes with high branching fraction such as $K^+e^-\bar{\nu}_e$ infeasible. Therefore, $K^+\pi^-$, $K^+\pi^-\pi^+\pi^-$ and $K^+\pi^-\pi^0$ hadronic flavor tag modes are utilized in this analysis to select the signal decay modes $D^0 \rightarrow K_{S,L}^0\pi^+\pi^-$. We account for the small DCS contamination of these hadronic flavor tags as part of the analysis. Note that inclusion of charge-conjugate processes is implied throughout unless stated otherwise.

Charged particles are reconstructed in the tracking system within the MDC acceptance $|\cos\theta| < 0.93$, where θ is the polar angle of the track with respect to the axis of the MDC (z -axis). For the charged particles that are direct products of the the D mesons, we require the distance of closest approach to the interaction point (IP) to be less than 1 cm in the $x - y$ plane and less than 10 cm along the z -axis. Whereas for the pion candidates used to reconstruct $K_S^0 \rightarrow \pi^+\pi^-$ decays, the only condition is on their distance to the IP along the z -axis, which is required to be less than 20 cm. We identify charged particles (PID) using combined probabilities from both time-of-flight information from the TOF and dE/dx measurements from the MDC under the pion and kaon hypotheses. The hypothesis with the greater combined probability is chosen and the charged particle is identified as a pion or a kaon accordingly.

To select photon candidates from showers in the EMC, we require energy deposits of at least 25 MeV in the barrel region of the EMC ($|\cos\theta| < 0.8$) and at least 50 MeV in the end-cap region ($0.86 < |\cos\theta| < 0.92$). Photon candidates must also be isolated from every charged track in an event by more than 10° to suppress the hadron interaction induced clusters in the EMC. Furthermore, to suppress clusters associated with either beam background or electronic noise, we require the time elapsed between the bunch crossing and the cluster's detection in the EMC is less than 700 ns. To reconstruct π^0 candidates, it is required that the invariant mass of a pair of photons lies within (0.110, 0.155) GeV/ c^2 . For better resolution, a kinematic fit is performed to constraint the di-photon mass to the nominal π^0 mass and the corresponding output four-momentum is utilized in the analysis.

Further selection is performed to suppress combinatorial backgrounds. We use two kinematic variables to identify tag and signal D mesons: the *energy difference* $\Delta E = \sqrt{s}/2 - E_D$ and the *beam-energy-constrained mass*,

$$M_{\text{BC}} = \sqrt{(\sqrt{s}/2)^2 - \sum_i |\mathbf{p}_i|^2}, \quad (4.1)$$

where E_D is the measured D meson energy and \mathbf{p}_i denotes the momentum vector of the i^{th} final state particle of the D meson under study. Signal decays peak at zero and the known D mass in the ΔE and M_{BC} distributions, respectively, whereas combinatorial background does not peak at all. The signal peak in the ΔE and M_{BC} distributions for the three tag-modes, $K^+\pi^-$, $K^+\pi^-\pi^+\pi^-$ and $K^+\pi^-\pi^0$ are modeled with double-Gaussian functions. Background distributions are described with polynomial and Argus functions [38] in the ΔE and M_{BC} distributions, respectively. Candidate D mesons are required to fall within intervals that are $\pm 3\sigma$ about the signal peaks of both ΔE and M_{BC} distributions. For events containing multiple tag-side D candidates satisfying all the conditions mentioned thus far, the combination with minimum $|\Delta E|$ is selected. To suppress the cosmic ray, Bhabha and di-muon background events in the $K^+\pi^-$ tag mode, two charged tracks, neither identified as an electron nor muon, with TOF time difference less than 5 ns are required. The $K^+\pi^-\pi^+\pi^-$ tag-mode decays contain a peaking background from $K_S^0 K^+\pi^-$ candidates with about 2% contamination rate, as estimated from the inclusive simulation sample. To suppress this background, a K_S^0 mass veto within the range [0.479, 0.518] GeV/ c^2 is applied on both permutations of oppositely charged pions selected in the $K^+\pi^-\pi^+\pi^-$ final state, reducing the $K_S^0 K^+\pi^-$ background to a negligible level of 0.09%.

For the $K_S^0\pi^+\pi^-$ signal mode, the number of charged particles passing all the conditions, apart from those used to reconstruct the tag decay, is required to be greater than or equal to four in an event. Candidate K_S^0 selection is performed in three steps while examining all possible combinations of the four selected charged tracks. Firstly, successive vertex fits are performed on the primary pions from D meson and the pair of pions being tested as final state particles coming from K_S^0 decays. The second step entails enforcing a K_S^0 mass window condition with 3σ bounds [0.485, 0.510] GeV/ c^2 on the the invariant mass of a pair of oppositely charged pions. Finally, a flight-significance criterion is placed wherein the decay length of the K_S^0 candidate is required to be greater than twice its uncertainty. Pion

tracks that are used to reconstruct K_S^0 candidates are not required to satisfy the particle identification criteria. Furthermore, events with multiple K_S^0 candidates are rejected to remove $D \rightarrow K_S^0 K_S^0 X$ decays.

To improve the momentum resolution, kinematic fits with all the final state particle momenta from both tag and signal sides are performed and the events for which the fit does not converge are discarded. Constraints related to the total four-momentum, D and K_S^0 masses are put in place. The signal efficiencies of the kinematic fit selection criteria for $K^+\pi^-$, $K^+\pi^-\pi^+\pi^-$ and $K^+\pi^-\pi^0$ tagged $K_S^0\pi^+\pi^-$ mode are 97.2%, 95.2% and 93.7% respectively.

In the $K_L^0\pi^+\pi^-$ signal selection, to suppress the $K_S^0\pi^+\pi^-$ peaking background, we require the number of charged particle tracks, that are not used to reconstruct the tag, to be exactly two, both of which must satisfy the above mentioned conditions of track selection. The residual four-momentum in the detector, called *missing-momentum*, after reconstructing all the charged tracks on the tag side and both the pion tracks on the signal side, is identified as a K_L^0 candidate; this method is referred to as the *missing-mass technique*. For both the signal modes, events containing a π^0 or η candidate are vetoed for which the invariant mass of any permutation of pairs of photons falls in the respective mass range of $[0.095, 0.165]$ GeV/c^2 and $[0.48, 0.58]$ GeV/c^2 . For the $K_L^0\pi^+\pi^-$ mode, the π^0 veto removes a significant fraction of the $D^0 \rightarrow K_S^0\pi^+\pi^-$ background, where $K_S^0 \rightarrow \pi^0\pi^0$. To determine the selection criteria on M_{BC} and ΔE for the $D \rightarrow K_S^0\pi^+\pi^-$ decays, we model both the distributions by performing maximum likelihood fits as shown in figure 3. The signal part in both ΔE and M_{BC} distributions is described by double Gaussian functions. The combinatorial background in the ΔE and M_{BC} distributions is modeled with polynomial and Argus functions, respectively. For the $K_L^0\pi^+\pi^-$ signal mode, a distribution of missing-mass squared defined as

$$M_{\text{miss}}^2 = (\sqrt{s}/2 - E_{\pi^+} - E_{\pi^-})^2 - |\mathbf{p}_{\text{tag}} + \mathbf{p}_{\pi^+} + \mathbf{p}_{\pi^-}|^2, \quad (4.2)$$

is analysed, where $(E_{\pi^\pm}, \mathbf{p}_{\pi^\pm})$ is the four-momentum of π^\pm candidates on the signal side and \mathbf{p}_{tag} is the total momentum of the single-tag D meson. The M_{miss}^2 distribution is modeled with double Gaussian functions for signal and peaking background, and a straight line for the combinatorial background. Candidates beyond a 3σ coverage about the mean, the bounds of which are given in table 3, are rejected in all the three kinematic variables. The total yields obtained after full reconstruction and selection are 16490 for the $K_S^0\pi^+\pi^-$ mode and 39085 for the $K_L^0\pi^+\pi^-$ mode.

Using signal simulation samples for $K_S^0\pi^+\pi^-$ and $K_L^0\pi^+\pi^-$ modes, average double-tag efficiencies over the DP for each tag mode are calculated and are given in table 4. Figure 4 shows the efficiency profile over the $K_L^0\pi^+\pi^-$ DP for the $K^+\pi^-$ tag mode as an example. The low momentum of pions at the edges of the DP cause these regions to have reduced efficiency.

Inclusive simulation samples from physics processes mentioned in section 3 are subjected to the same event-selection criteria as in data. Negligible background is retained with the $K_S^0\pi^+\pi^-$ sample due to the requirement that the six-constraint kinematic fit is successful. However, the $K_L^0\pi^+\pi^-$ selection criteria allow for about (10 – 12)% background

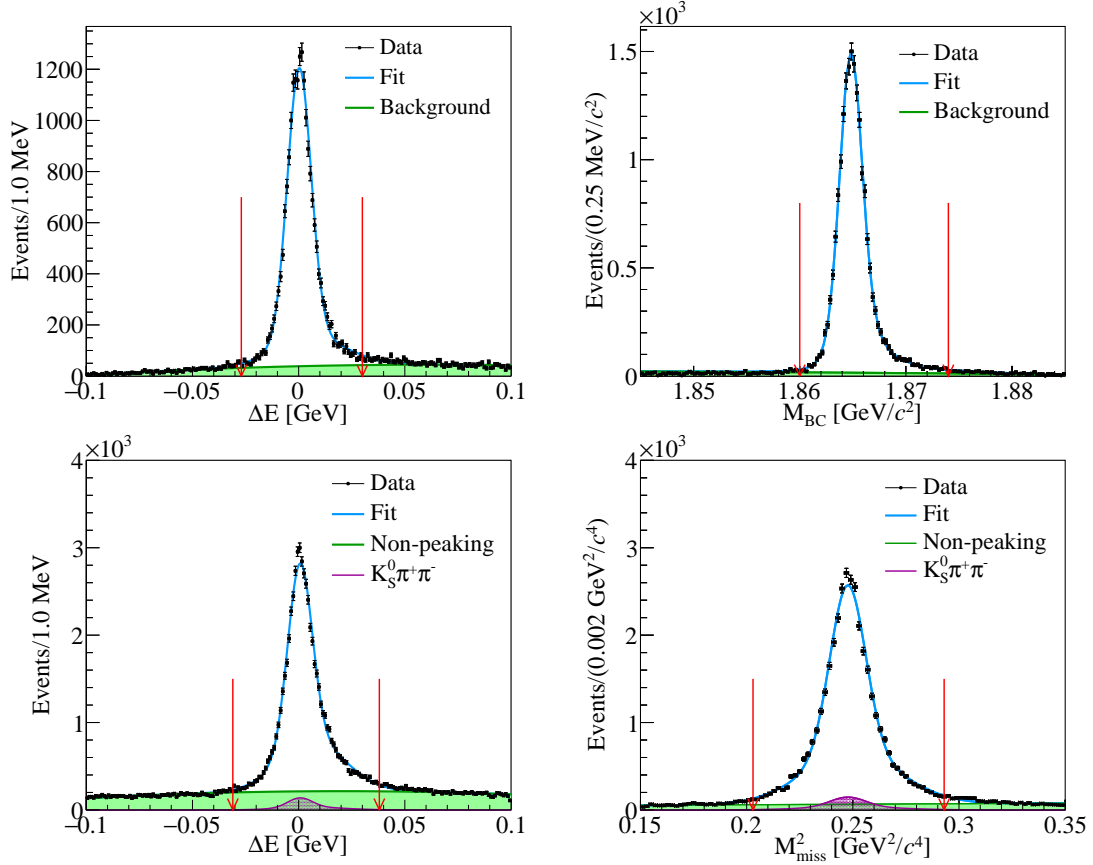


Figure 3: The ΔE , M_{BC} distributions for $K_S^0\pi^+\pi^-$ signal candidates (*top*) and ΔE , M_{miss}^2 distributions for $K_L^0\pi^+\pi^-$ signal candidates (*bottom*) in data. The red arrows indicate the allowed signal regions.

Variable	$K_S^0\pi^+\pi^-$	$K_L^0\pi^+\pi^-$
ΔE [GeV]	$[-0.027, 0.030]$	$[-0.031, 0.038]$
M_{BC} [GeV/c^2]	$[1.860, 1.874]$	—
M_{miss}^2 [GeV^2/c^4]	—	$[0.203, 0.293]$

Table 3: Signal ΔE , M_{BC} and M_{miss}^2 selection bounds in data.

contamination for the three tag modes as summarized in table 4, of which approximately 5% is $K_S^0\pi^+\pi^-$, which peaks in the M_{miss}^2 distribution. The remaining non-peaking background constitutes a number of hadronic and semi-leptonic modes. Modeling of these background events in the amplitude analysis is described in section 5.

	$\epsilon_{\text{avg}}^{DT} [\%]$		$K_L^0\pi^+\pi^-$ vs. tag contamination rates [%]	
Tag	$K_S^0\pi^+\pi^-$	$K_L^0\pi^+\pi^-$	Non-peaking background	$K_S^0\pi^+\pi^-$ background
$K\pi$	25.85 ± 0.02	35.89 ± 0.02	5.96 ± 0.08	4.79 ± 0.07
$K\pi\pi\pi$	12.25 ± 0.02	14.31 ± 0.01	5.84 ± 0.10	4.07 ± 0.07
$K\pi\pi^0$	13.02 ± 0.01	17.77 ± 0.01	6.48 ± 0.06	4.86 ± 0.05

Table 4: Average double-tag efficiencies for $K_S^0\pi^+\pi^-$ and $K_L^0\pi^+\pi^-$ signal modes.

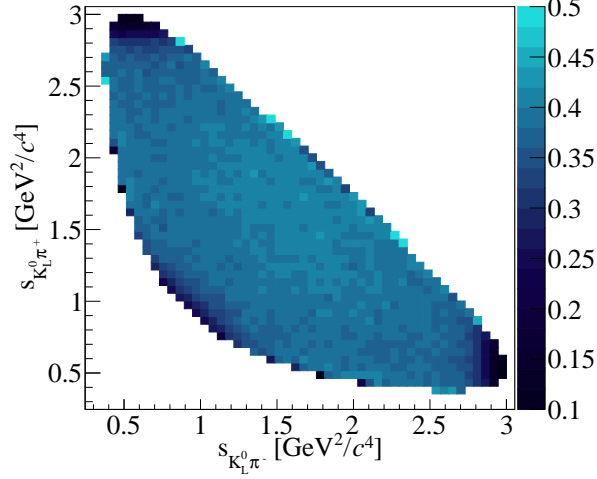


Figure 4: The DT efficiency profile for $K_L^0\pi^+\pi^-$ signal mode tagged with the $K\pi$ candidate.

5 Amplitude analysis

The strategy adopted is to fit the $K_S^0\pi^+\pi^-$ sample alone to validate the fitter, then this sample is used as a constraint in a simultaneous fit with the $K_L^0\pi^+\pi^-$ sample to determine $\hat{\rho}_{k_{CP}}$. The signal probability distribution function (PDF) at a phase-space point \mathbf{x} is expressed in terms of the total amplitude $\mathcal{A}_{\text{sig}}(\mathbf{x})$ obtained from the isobar model discussed in section 2 and the detector efficiency $\epsilon(\mathbf{x})$:

$$p_{\text{sig}}(\mathbf{x}) = \frac{\epsilon(\mathbf{x})|\mathcal{A}_{\text{sig}}(\mathbf{x})|^2}{\int_D \epsilon(\mathbf{x})|\mathcal{A}_{\text{sig}}(\mathbf{x})|^2 d\mathbf{x}} = \frac{\epsilon(\mathbf{x})|\mathcal{A}_{\text{sig}}(\mathbf{x})|^2}{\mathcal{N}_{\text{sig}}}, \quad (5.1)$$

where the normalization integral \mathcal{N}_{sig} is over the DP and is calculated using *Monte Carlo (MC) integration* [39], wherein the integral can be approximated as a discrete summation of the signal PDF over a large number of phase-space points N called the *integration sample*:

$$\mathcal{N}_{\text{sig}} \approx \frac{1}{N} \sum_{j=0}^N \frac{\epsilon(\mathbf{x}_j)}{q(\mathbf{x}_j)} |\mathcal{A}_{\text{sig}}(\mathbf{x}_j)|^2. \quad (5.2)$$

The integration sample is distributed as the PDF $q(\mathbf{x})$ at the end of sample generation, reconstruction and selection and therefore can be related to the generator level PDF $Q(\mathbf{x})$

as: $q(\mathbf{x}) = \epsilon(\mathbf{x})Q(\mathbf{x})$. This allows cancellation of the explicit dependence on the efficiency of the normalization factor which can be written as,

$$\mathcal{N}_{\text{sig}} = \frac{1}{N} \sum_{j=0}^N \frac{|\mathcal{A}_{\text{sig}}(\mathbf{x}_j)|^2}{Q(\mathbf{x}_j)}. \quad (5.3)$$

The total PDF accounting for signal and background incoherently with appropriate weights is

$$\mathcal{P}(\mathbf{x}) = (1 - w_{K_S} - w_{\text{np}})p_{\text{sig}}(\mathbf{x}) + w_{K_S}p_{K_S}(\mathbf{x}) + w_{\text{np}}p_{\text{np}}(\mathbf{x}), \quad (5.4)$$

where p_{K_S} and p_{np} are the PDFs describing $K_S^0\pi^+\pi^-$ peaking background and the non-peaking background with weights w_{K_S} and w_{np} respectively. A negative log-likelihood function is constructed as

$$-2\log\mathcal{L}' = -2\log \prod_{i \in \text{data}} \mathcal{P}(\mathbf{x}_i) = -2 \sum_{i \in \text{data}} \log \mathcal{P}(\mathbf{x}_i). \quad (5.5)$$

Since the reconstruction efficiencies are independent of the parameters to be estimated, they can be factored out and an effective likelihood function \mathcal{L} can be defined as

$$-2\log\mathcal{L} = -2 \sum_{i \in \text{data}} \log \mathcal{P}(\mathbf{x}_i) + 2 \sum_{i \in \text{data}} \log\epsilon(\mathbf{x}_i); \quad (5.6)$$

$$-2\log\mathcal{L} = -2 \sum_{i \in \text{data}} \log \left[(1 - w_{K_S} - w_{\text{np}}) \frac{|\mathcal{A}_{\text{sig}}(\mathbf{x}_i)|^2}{\mathcal{N}_{\text{sig}}} + w_{K_S} \frac{|\mathcal{A}_{K_S}(\mathbf{x}_i)|^2}{\mathcal{N}_{K_S}} + w_{\text{np}} \frac{|\mathcal{A}_{\text{np}}(\mathbf{x}_i)|^2}{\mathcal{N}_{\text{np}}} \right], \quad (5.7)$$

which can be minimized, without any efficiency function as an input, to obtain the parameters of interest (a_r, ϕ_r) introduced in section 2. Here, \mathcal{N}_{K_S} and \mathcal{N}_{np} are the normalization factors calculated using the $K_S^0\pi^+\pi^-$ and non-peaking background model descriptions on events generated with $K_L^0\pi^+\pi^-$ reconstruction and selection efficiency effects.

The peaking background PDF p_{K_S} can be described by the same amplitude model as would be applied to the $K_S^0\pi^+\pi^-$ signal acting as a constraint in the $K_L^0\pi^+\pi^-$ fit. The non-peaking background PDF is described using the *side-bands*, *i.e.* regions dominated by background away from the signal, of the M_{miss}^2 distribution. The width and position of the side-bands are optimized using the inclusive MC simulation sample with a χ^2 statistic for maximum compatibility with the non-peaking background distribution in the signal region. The upper and lower side-band regions are defined by the limits $[0.107, 0.173] \text{ GeV}^2/c^4$ and $[0.323, 0.350] \text{ GeV}^2/c^4$, respectively. A two-dimensional Gaussian kernel estimator [40] is used to model the background distribution in the side-bands. The projections of the resultant PDF are shown in figure 5. Any difference between the distribution of background over the DP in the sideband and the signal region is considered as a source of systematic uncertainty.

We account for two additional effects in the fit. Firstly, we correct for the fact that hadronic decays of the $D^0 \rightarrow K^-X$, where X are combinations of pions on the tag side, are not an exact flavour tag. This effect comes from a contamination by tag-side DCS decays of type $D^0 \rightarrow K^+X$, $\bar{D}^0 \rightarrow K_{S/L}^0\pi^+\pi^-$. An event tagged by a DCS decay will

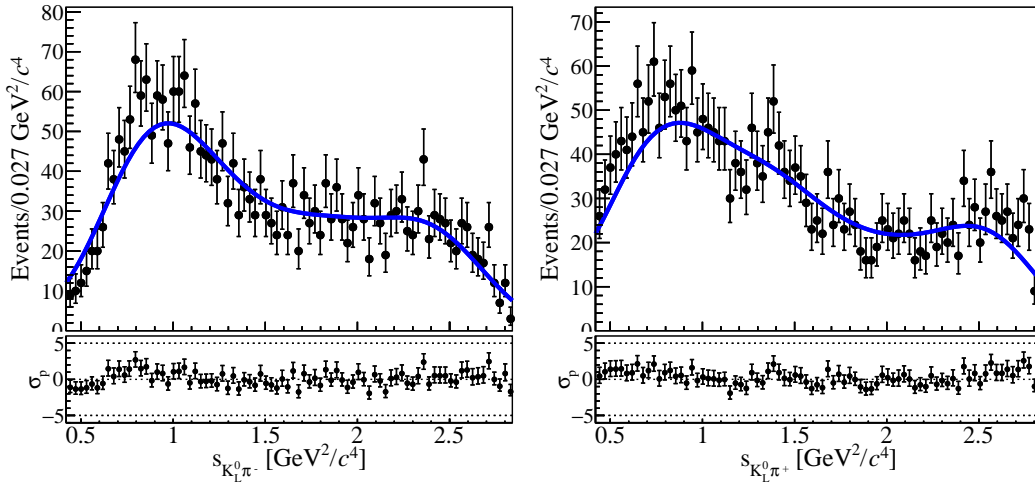


Figure 5: Distributions of $s_{K_L^0 \pi^-}$ and $s_{K_L^0 \pi^+}$ for candidates in the M_{miss}^2 sidebands (black dots) in data. The fit PDF (blue) is superimposed.

incorrectly place the signal $K_{S/L}^0 \pi^+ \pi^-$ at $(s_{K_L^0 \pi^-}, s_{K_L^0 \pi^+})$ rather than $(s_{K_L^0 \pi^+}, s_{K_L^0 \pi^-})$. These DCS-tagged events can be accounted for by adding their amplitudes to the nominal CF pure-flavor-tag amplitude coherently as

$$\mathcal{A} = \mathcal{A}_F \bar{\mathcal{A}}_{\bar{G}} - \bar{\mathcal{A}}_{\bar{F}} \mathcal{A}_G, \quad (5.8)$$

where $\mathcal{A}_F (\bar{\mathcal{A}}_{\bar{F}})$ is the amplitude of the signal decay $D^0 (\bar{D}^0) \rightarrow K_S^0 \pi^+ \pi^-$ and $\bar{\mathcal{A}}_{\bar{G}} (\mathcal{A}_G)$ is the amplitude of the tag mode $\bar{D}^0 (D^0) \rightarrow K^+ \pi^-$. The decay probabilities integrated over the allowed tag mode phase-space, at position \mathbf{x} on the $K_S^0 \pi^+ \pi^-$ and $K_L^0 \pi^+ \pi^-$ DPs, are given by

$$|\mathcal{A}(\mathbf{x})|_{K_S^0 \pi \pi}^2 = \left(|\mathcal{A}_F(\mathbf{x})|^2 + (r_D^G)^2 |\bar{\mathcal{A}}_{\bar{F}}(\mathbf{x})|^2 - 2r_D^G R_G \mathcal{R}e[e^{-i\delta_G} \mathcal{A}_F^*(\mathbf{x}) \bar{\mathcal{A}}_{\bar{F}}(\mathbf{x})] \right), \quad (5.9)$$

$$|\mathcal{A}(\mathbf{x})|_{K_L^0 \pi \pi}^2 = \left(|\mathcal{A}_F(\mathbf{x})|^2 + (r_D^G)^2 |\bar{\mathcal{A}}_{\bar{F}}(\mathbf{x})|^2 + 2r_D^G R_G \mathcal{R}e[e^{-i\delta_G} \mathcal{A}_F^*(\mathbf{x}) \bar{\mathcal{A}}_{\bar{F}}(\mathbf{x})] \right), \quad (5.10)$$

where the parameter r_D^G is the DCS to CF amplitude ratio and $R_G e^{-i\delta_G}$ measures the coherence between them for the tag mode G . The last terms in eqs. 5.9 and 5.10 contain the interference between CF and DCS amplitudes, which dominates the tag-side DCS effects in the total-decay probability. The values used for the hadronic parameters for the three tag modes involved in this analysis are from the Refs. [41] and [42] and are listed in table 5.

Secondly, we account for differences in the acceptance between the experimental data and the simulated events used to normalize the PDFs. Any difference is accounted for in the total PDF by scaling the normalization factor by ratios of reconstruction efficiencies in data ϵ^{data} and simulated events ϵ^{sim} , obtained by studying BESIII control samples, for each of the final state particles in the signal mode. These scale factors denoted by γ_ϵ are

G	r_D^G [%]	δ_G [°]	R_G
$K\pi$	5.867 ± 0.015	$190.0^{+4.2}_{-4.1}$	1
$K\pi\pi\pi$	5.50 ± 0.07	161^{+28}_{-18}	$0.44^{+0.10}_{-0.09}$
$K\pi\pi^0$	4.41 ± 0.11	196 ± 11	0.79 ± 0.04

Table 5: DCS to CF amplitude ratios and coherence parameters [41, 42].

defined as

$$\gamma_\epsilon = \prod_i \frac{\epsilon_i^{\text{data}}(p_i)}{\epsilon_i^{\text{sim}}(p_i)}, \quad (5.11)$$

where p_i is momentum of the decay particle $i \in \{K_{S/L}^0, \pi^+, \pi^-\}$. The contributions to the correction for pions arise from both PID and tracking efficiency differences. The γ_ϵ factor variations with momentum are parametrized using various polynomial and exponential functions and the net correction in the normalisation factor defined in eq. 5.3 appears as,

$$\mathcal{N} = \frac{1}{N} \sum_{j=0}^N \gamma_\epsilon(p_j^{K^0}, p_j^{\pi^+}, p_j^{\pi^-}) |\mathcal{A}(\mathbf{x}_j)|^2, \quad (5.12)$$

where, $p_j^{K^0}$, $p_j^{\pi^+}$ and $p_j^{\pi^-}$ are the momenta of $K_{S/L}$, π^+ and π^- at point \mathbf{x} on the DP, respectively.

Previous $K_S^0\pi^+\pi^-$ amplitude-model analysis based on Belle and BABAR data suggests eleven Breit-Wigner P and D wave resonances, two $K\pi$ S-wave and a broad $\pi\pi$ S-wave contribution to the three-body decay [15]. However, the BESIII data sample is two orders of magnitude smaller than the combined Belle and BABAR data set, which means there is no sensitivity to some of the components. We assign significance to each of the contributions as p-values from χ^2 distributions, approximated using Wilk's theorem [43], from the ratios of generalized log-likelihood values, calculated with and without the resonant contribution under test. The significance values for both the scenarios against each of the test resonance are given in table 6. The resonance $\rho(770)$ is considered as the reference relative to which all other resonance amplitudes are measured. In a standalone $K_S^0\pi^+\pi^-$ amplitude fit, the resonances $K^*(1680)^-$, $K^*(892)^+$, $K_2^*(1430)^+$, $K^*(1410)^+$ and $K_0^*(1430)^+$ are observed to be statistically insignificant, whereas upon including the $K_L^0\pi^+\pi^-$ mode in the fit, only the DCS $K_0^*(1430)^+$ has a significance below 3σ .

The first validation of the fitter is carried out by generating an ensemble of 350 simulated $K_S^0\pi^+\pi^-$ and $K_L^0\pi^+\pi^-$ event samples based on a fitted model as is described in section 6 ahead, which are fit to compare the measured and generated model parameters. Each generated sample has the same size as the data sample. The $K_L^0\pi^+\pi^-$ samples contain DCS as well as background contamination in the same proportion as data for all the three tag modes. The K -matrix parameters are global parameters and their values are known from the large Belle-BABAR data sample [15]. Therefore, the K -matrix description is kept

Resonance	$[K_S^0\pi^+\pi^-]$	$[K_L^0\pi^+\pi^-, K_S^0\pi^+\pi^-]$
$K^0\rho(770)$	–	–
$K^0\omega(782)$	5.1	8.8
$K^0f_2(1270)$	7.3	11.9
$K^0\rho(1450)$	4.2	12.1
$K^*(892)^-\pi^+$	86.3	168.9
$K_2^*(1430)^-\pi^+$	12.4	19.1
$K^*(1680)^-\pi^+$	1.7	5.7
$K^*(1410)^-\pi^+$	4.2	3.7
$K^*(892)^+\pi^-$	0.5	17.0
$K_2^*(1430)^+\pi^-$	2.0	4.3
$K^*(1410)^+\pi^-$	1.1	2.9
$K_0^*(1430)^-\pi^+$	20.1	37.1
$K_0^*(1430)^+\pi^-$	1.1	2.0
$\pi^+\pi^-$ S-wave	32.1	52.8

Table 6: Significance values of resonant components for standalone $K_S^0\pi^+\pi^-$ and simultaneous $K_L^0\pi^+\pi^-$, $K_S^0\pi^+\pi^-$ model fits.

fixed in all the fits. Distributions of the difference between input and output model parameters divided by their uncertainty are produced and found to be consistent with a normal distribution.

The second validation is to compare to the results of Ref. [15]. Therefore, we perform the analysis on a $K_S^0\pi^+\pi^-$ candidates only. The fit model is compared against data as the DP projections and is shown in figure 6. The goodness of fit is measured with a reduced χ^2 statistic and is observed to be equal to 0.97 for the toy model fit. To further validate the fit, we determine the fit fractions of our model. In contrast to the amplitude formalism dependent fit parameters a_r and ϕ_r , the fractional contribution of each component to the total decay probability, called *fit fraction*, is expected to be a consistent global physics parameter for a particular multibody decay. The functional form of the fit fraction for a resonant contribution R is given by,

$$FF_R = \frac{\int d\mathbf{x} |\mathcal{A}_R(\mathbf{x})|^2}{\int d\mathbf{x} |\sum_r \mathcal{A}_r(\mathbf{x})|^2}. \quad (5.13)$$

An aggregate of the fit fractions away from 100% suggests interference effects. The predicted fit fractions of various components show reasonable agreement with the Belle-BABAR values as also shown in table 7.

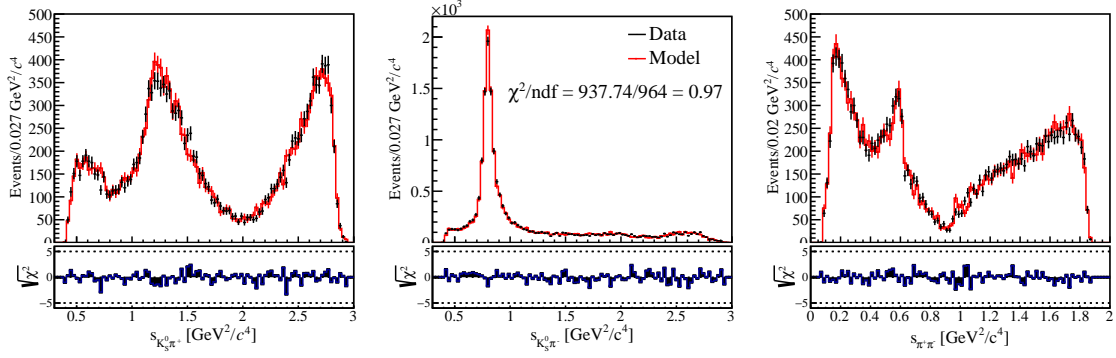


Figure 6: DP projections of $K_S^0 \pi^+ \pi^-$ data event distribution and model prediction from a standalone $K_S^0 \pi^+ \pi^-$ fit.

Resonance	Belle-BABAR FF_R [%]	Predicted FF_R [%]
$K_S^0 \rho(770)^0$	20.4	$17.2^{+1.8}_{-1.9}$
$K_S^0 \omega(782)$	0.5	$0.3^{+0.3}_{-0.1}$
$K_S^0 f_2(1270)$	0.8	$0.7^{+0.7}_{-0.8}$
$K_S^0 \rho(1450)^0$	0.6	$0.8^{+1.1}_{-1.2}$
$K^*(892)^- \pi^+$	59.9	$58.9^{+6.7}_{-3.6}$
$K_2^*(1430)^- \pi^+$	1.3	$2.1^{+0.2}_{-0.4}$
$K^*(1680)^- \pi^+$	0.5	0.52 ± 0.02
$K^*(1410)^- \pi^+$	0.1	0.020 ± 0.001
$K^*(892)^+ \pi^-$	0.6	0.54 ± 0.01
$K_2^*(1430)^+ \pi^-$	< 0.1	0.011 ± 0.001
$K^*(1410)^+ \pi^-$	< 0.1	0.0304 ± 0.0001
$\pi^+ \pi^-$ S -wave	10.0	$8.2^{+1.0}_{-0.5}$
$K_0^*(1430)^- \pi^+$	7.0	$8.2^{+1.0}_{-2.2}$
$K_0^*(1430)^+ \pi^-$	< 0.1	0.0084 ± 0.0002
Total	101.6	$100.2^{+12.8}_{-10.7}$

Table 7: Comparison of predicted fit fractions from the standalone $K_S^0 \pi^+ \pi^-$ model with Belle-BABAR results.

Resonance	a_r	ϕ_r [°]
$\rho(770)$	1.0	0.0
$\omega(782)$	0.0388 ± 0.0031	105.1 ± 5.3
$f_2(1270)$	1.30 ± 0.13	-41.2 ± 4.4
$\rho(1450)$	1.69 ± 0.40	109.9 ± 8.2
$K^*(892)^-$	1.84 ± 0.03	138.3 ± 1.2
$K_2^*(1430)^-$	1.50 ± 0.05	-48.0 ± 2.1
$K^*(1680)^-$	2.32 ± 0.28	-191.5 ± 9.4
$K^*(1410)^-$	0.48 ± 0.07	-143.0 ± 7.6
$K^*(892)^+$	0.16 ± 0.01	-36.2 ± 3.6
$K_2^*(1430)^+$	0.25 ± 0.05	-86.6 ± 10.9
$K^*(1410)^+$	0.23 ± 0.05	68.5 ± 12.9
$K_0^*(1430)^-$	2.39 ± 0.06	97.7 ± 1.4

Table 8: Amplitude parameters (a_r, ϕ_r) predicted from the simultaneous fit.

6 Results

The results are obtained from a simultaneous fit to the combined sample of $K_S^0\pi^+\pi^-$ and $K_L^0\pi^+\pi^-$ data candidates. The fit minimizes the negative log-likelihood function composed of the PDFs given in eqs. 5.9 and 5.10, which include all the statistically significant (greater than 3σ) components listed in table 6, as well as incorporating the multiplicative factors related to the U-spin breaking parameters for the CP resonances, described in section 2. The peaking background fraction is fixed to the values obtained from simulated events, whereas the non-peaking background fractions are constrained with an additional χ^2 term in the likelihood function, composed of weighted difference between MC simulated values and the values to be estimated. Uncertainties associated with both assumptions are considered as systematic uncertainties. The amplitude and U-spin breaking parameters are presented in tables 8 and 9, respectively. The modulus of the $\hat{\rho}$ parameters notably lie in a wide range of values from 0.4 for the $\pi\pi$ S-wave to 12.1 for the $\rho(1450)$ resonance and the phases are in general measured to be away from 0° for all the CP resonances.

DP projections of the predicted model compared to data for $K_L^0\pi^+\pi^-$ and $K_S^0\pi^+\pi^-$ modes are given in figures 7 and 8, respectively. The reduced χ^2 , after ensuring statistical significance in each 2D phase-space bin through combining adjacent bins, is found to be $1969.2/1790 = 1.10$ for $K_L^0\pi^+\pi^-$ and $829.2/966 = 0.86$ for $K_S^0\pi^+\pi^-$ mode, suggesting that the model describes the data reasonably well. Small deviations are observed in the $\rho(770) - \omega(782)$ interference region. The DCS interference in a $K_L^0\pi^+\pi^-$ model has overall constructive effects as opposed to an overall destructive interference in a $K_S^0\pi^+\pi^-$ model.

Resonance	$ \hat{\rho} $	$\arg(\hat{\rho})$ [°]	$ 1 - 2\tan^2\theta_C\hat{\rho} ^2$
$\rho(770)$	$1.93 \pm 0.27 \pm 0.42$	$-90.6 \pm 5.8 \pm 7.6$	$1.05 \pm 0.04 \pm 0.06$
$\omega(782)$	$6.13 \pm 0.75 \pm 0.53$	$2.2 \pm 7.0 \pm 4.8$	$0.12 \pm 0.05 \pm 0.04$
$f_2(1270)$	$3.75 \pm 0.90 \pm 0.81$	$-56.5 \pm 16.8 \pm 12.9$	$0.72 \pm 0.20 \pm 0.15$
$\rho(1450)$	$12.12 \pm 2.92 \pm 1.88$	$78.4 \pm 14.4 \pm 15.6$	$2.19 \pm 0.95 \pm 0.83$
$\pi\pi$ S-wave	$0.37 \pm 0.21 \pm 0.37$	$-164.4 \pm 15.7 \pm 13.4$	$1.08 \pm 0.04 \pm 0.08$

Table 9: Measured U-spin breaking parameters. The first uncertainty is statistical and the second is total systematic.

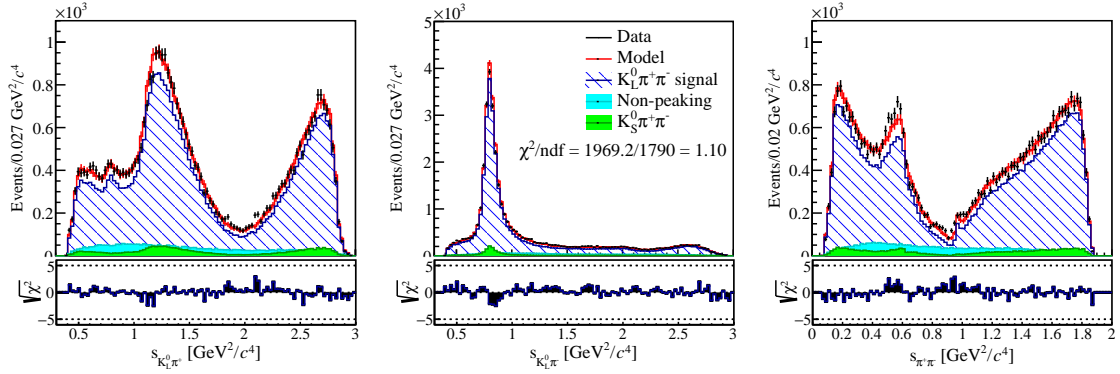


Figure 7: Model and data DP projections of $K_L^0\pi^+\pi^-$ signal mode.

This effect results in the lower total fit fraction and in the partial-fit fractions of some CF components, such as $K^*(892)^-$ and $K_0^*(1430)^-$ for a $K_L^0\pi^+\pi^-$ model as compared to $K_S^0\pi^+\pi^-$. The CP -resonance fit fractions are additionally affected by the U-spin breaking parameter phases, of which the $\omega(782)$ resonance is a clear example. Fit fraction for both the modes are given in table 10.

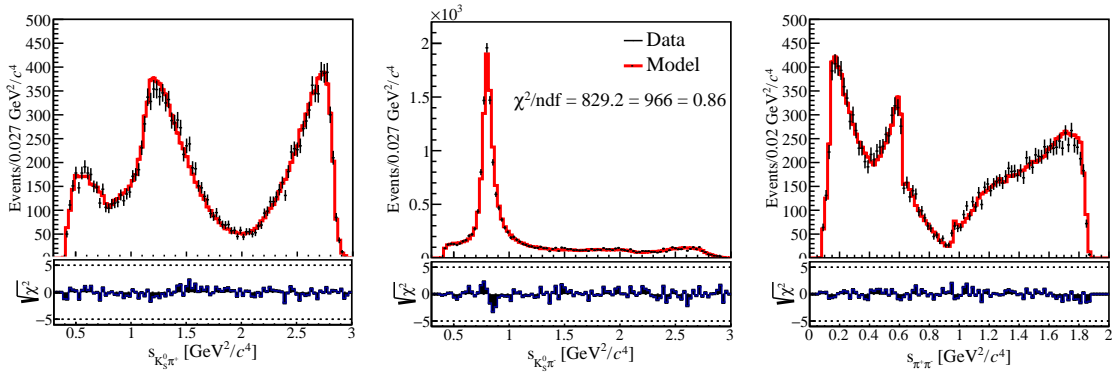


Figure 8: Model and data DP projections of $K_S^0\pi^+\pi^-$ signal mode.

Model-predicted strong-phase parameter values for $K_L^0\pi^+\pi^-$ and $K_S^0\pi^+\pi^-$, in equal-

Resonance	$K_L^0 \pi^+ \pi^- FF_R$ [%]	$K_S^0 \pi^+ \pi^- FF_R$ [%]
$\rho(770)$	$18.16^{+0.53}_{-0.45} \pm 2.50$	$18.90 \pm 0.42 \pm 2.12$
$\omega(782)$	$0.06^{+0.03}_{-0.02} \pm 0.04$	$0.54 \pm 0.09 \pm 0.14$
$f_2(1270)$	$0.40 \pm 0.08 \pm 0.37$	$0.61^{+0.13}_{-0.11} \pm 0.29$
$\rho(1450)$	$0.42 \pm 0.08 \pm 0.53$	$0.21 \pm 0.10 \pm 0.40$
$K^*(892)^-$	$56.98^{+0.58}_{-0.56} \pm 3.10$	$62.18^{+0.55}_{-0.59} \pm 2.58$
$K_2^*(1430)^-$	$1.64^{+0.10}_{-0.09} \pm 0.48$	$1.79 \pm 0.09 \pm 0.47$
$K^*(1680)^-$	$0.25^{+0.06}_{-0.05} \pm 0.68$	$0.27 \pm 0.06 \pm 0.63$
$K^*(1410)^-$	$0.19 \pm 0.06 \pm 0.46$	$0.21 \pm 0.06 \pm 0.19$
$K^*(892)^+$	$0.45 \pm 0.05 \pm 0.14$	$0.49 \pm 0.05 \pm 0.35$
$K_2^*(1430)^+$	$0.05 \pm 0.02 \pm 0.04$	$0.05 \pm 0.02 \pm 0.03$
$K^*(1410)^+$	$0.04 \pm 0.02 \pm 0.03$	$0.05 \pm 0.02 \pm 0.02$
$K_0^*(1430)^-$	$6.84^{+0.24}_{-0.25} \pm 1.84$	$7.47 \pm 0.26 \pm 1.55$
$\pi\pi$ S-wave	$10.12^{+0.32}_{-0.33} \pm 0.96$	$10.24 \pm 0.23 \pm 1.62$
Total	$95.59^{+2.16}_{-2.07} \pm 11.17$	$103.02^{+2.11}_{-2.10} \pm 10.39$

Table 10: $D^0 \rightarrow K_{L,S}^0 \pi^+ \pi^-$ fit fractions from the simultaneous amplitude fit.

$\Delta\delta_D$ binning, are presented in figure 9, along with statistical error coverage up to three standard deviations. Model-independent and Belle-BABAR $K_S^0 \pi^+ \pi^-$ model [15] predicted values are also shown for comparison. These show good agreement with the model-independent measurements, with the reduced χ^2 values of 1.12 for (c_i, s_i) and 0.21 for (c'_i, s'_i) , weighted by both statistical and systematic uncertainties.

As part of robustness tests on the amplitude model, various crosschecks on the amplitude fit are performed. The nominal isobar model for $\rho(770)$ and $\omega(782)$ is replaced with a $\rho - \omega$ mixing model with $\rho(770)$ parametrized by a Gounaris-Sakurai lineshape [44] instead of the relativistic Breit-Wigner. The fit yields worse agreement with data at the $\rho(770)$ peak and in the $\rho(770) - \omega(782)$ interference region and therefore the nominal isobar model is preferred.

Separate fits on data subdivided by tag-mode are performed. The resultant U-spin breaking parameters from all the three optimizations agree with the main fit results within uncertainties and are provided in appendix B. An additional test is performed by modeling the $K_L^0 \pi^+ \pi^-$ data independently without using the $K_S^0 \pi^+ \pi^-$ data as a constraint. The procedure and the results are provided in appendix C.

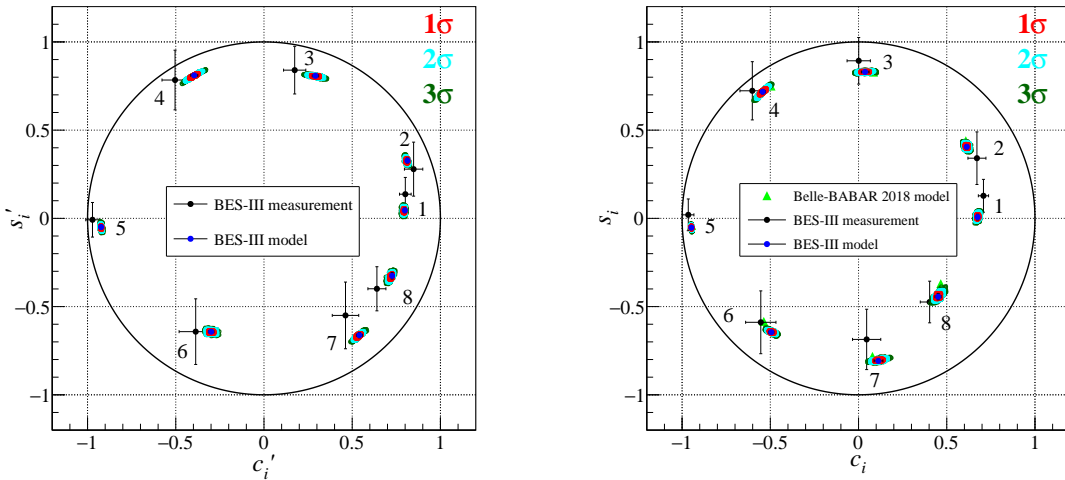


Figure 9: (*Left*) Strong-phase parameters c'_i and s'_i predicted using the $K_L^0\pi^+\pi^-$ model from this analysis, compared against the model-independent BESIII measurements [15]. (*Right*) Strong-phase parameters c_i and s_i predicted using the $K_S^0\pi^+\pi^-$ model from this analysis, compared against the model-independent BESIII measurements and the Belle model-predicted values.

7 Systematic uncertainty

Several sources of systematic uncertainty are explored. Parameters that are kept fixed in the fit are the dominant contribution; the next largest contributions come from experimental effects such as acceptance.

The fixed parameters include masses and widths of the resonant states, the K -matrix coupling parameters β_α and f_{1i}^{prod} for four poles and four channels, LASS resonant and non-resonant relative magnitudes and phases, the effective radii, and the tag mode DCS to CF ratios and coherence factors. Uncertainties due to these are calculated by performing repeated simultaneous $K_S^0\pi^+\pi^-$ and $K_L^0\pi^+\pi^-$ data fits on smeared values of the concerned fixed parameter within its uncertainty. Fixed central values and uncertainties on masses, widths and meson radii are taken from the PDG, on K -matrix and LASS parameters from the results of Belle-BABAR analysis [15], and the latest LHCb [41] and BESIII [42] results are used for the hadronic decay parameters of the tag modes. As the uncertainties on the meson radii are actually ignorance on their values, as there have been no experimental measurements, their smearing is uniform. Central values used for effective radii for the resonances is 1.5 GeV^{-1} and for the D meson is 5 GeV^{-1} , and the ignorance is valued at $\pm 1 \text{ GeV}^{-1}$ for both. Gaussian smearing is employed for the rest of the fixed parameters.

The effects of uncertainty associated with the difference in acceptance of data and simulated events parametrized by the γ_ϵ factor is studied. Binned uncertainties for pion and kaon PID and tracking efficiency, as well as $K_{S,L}^0$ reconstruction efficiencies are taken from the control sample studies mentioned in section 5. We perform data fits varying the values of γ_ϵ by one standard deviation and the variations in the fit parameters are used to

assign uncertainties from this source.

Minor contributions to the systematic uncertainty are associated with the peaking-background fraction (w_{K_S}) and the non-peaking background description on the phase-space. Uncertainty on the peaking background fraction comes from the size of the simulated sample, which is less than 0.1% absolute and $K_S^0 \rightarrow K_L^0$ mis-ID rate, calculated by reconstructing $K_S^0 \rightarrow \pi^0\pi^0$ in data using a J/ψ control sample, is about 4.5% of w_{K_S} . To calculate the uncertainty associated with the modeling of the non-peaking background on the phase-space, pseudo-experiment $K_L^0\pi^+\pi^-$ data samples are generated wherein the non-peaking background component is modeled from the M_{miss}^2 signal region in the simulated sample. Amplitude fits are performed on these pseudo-experiment samples with non-peaking background descriptions based first on the actual signal region background events and then on the sideband event distributions. Any departure observed in the output values of these two cases is assigned as the systematic uncertainty from this source and is of the order of a percent for the U-spin breaking parameters.

The total systematic uncertainty is obtained by adding all the sources in quadrature and is found to be of a similar size to the statistical uncertainties for the U-spin breaking parameters. The fit fractions carry significantly larger systematic uncertainty as compared to statistical. The systematic uncertainties on U-spin breaking parameters, fit fractions and strong-phase parameters due to each source are given in appendix D.

8 CP content and BF ratio

Functional form of the decay amplitudes on the phase-space of the $K_S^0\pi^+\pi^-$ and $K_L^0\pi^+\pi^-$ final states can be exploited to calculate the CP even fraction of both the states and the ratio of their branching fractions. The CP even fraction of a multi-particle state like $K_L^0\pi^+\pi^-$ is defined as [45],

$$F_{CP} = \frac{M_+}{M_+ + M_-} = \frac{1}{2} - C\sqrt{F\bar{F}}, \quad (8.1)$$

where $M_{+(-)}$ is the decay probability of D^0 into $K_L^0\pi^+\pi^-$ in a CP even(odd) state and C is the weighted average of cosine of the associated strong-phase difference over the entire phase-space and an unbinned version of eq. 2.1. F and \bar{F} are the fractions of flavor-tagged $D^0 \rightarrow K_L^0\pi^+\pi^-$ and $\bar{D}^0 \rightarrow K_L^0\pi^+\pi^-$ yields, respectively. A similar treatment can be applied to $K_S^0\pi^+\pi^-$ state by adding the $C\sqrt{F\bar{F}}$ factor to 0.5. The model predicted F_{CP} value for $K_L^0\pi^+\pi^-$ state is found to be $35.3 \pm 0.6_{(\text{stat.})} \pm 1.4_{(\text{syst.})}\%$ and for $K_S^0\pi^+\pi^-$ $55.6 \pm 0.6_{(\text{stat.})} \pm 1.2_{(\text{syst.})}\%$. These results agree with the values 35.2% for $K_L^0\pi^+\pi^-$ and 55.2% for $K_S^0\pi^+\pi^-$ calculated from Ref. [18] with measured CP yields in a model-independent approach. This suggests that the state $K_L^0\pi^+\pi^-$ is significantly CP odd in contrast to the $K_S^0\pi^+\pi^-$ state, which is approximately CP neutral.

Finally, the ratio of branching fractions of $D^0 \rightarrow K_L^0\pi^+\pi^-$ and $D^0 \rightarrow K_S^0\pi^+\pi^-$ decay modes from a model can be calculated by dividing the respective total decay probabilities on a common phase-space distribution, and is evaluated as $1.091 \pm 0.012_{(\text{stat.})} \pm 0.032_{(\text{syst.})}$. This is in good agreement with the corresponding number from a model-independent analysis, which is estimated to be $1.105 \pm 0.012_{(\text{stat.})} \pm 0.015_{(\text{syst.})}$ using inputs from Refs. [18, 19].

9 Conclusion

Using quantum-correlated $D\bar{D}$ pairs, the first data-driven determination of the U-spin breaking parameters associated with the decay $D^0 \rightarrow K_L^0\pi^+\pi^-$ is reported. The measured values for all the CP -resonant modes show significant deviations from the nominally assumed value of unity. For all resonant modes, we place tighter bounds on $[|\hat{\rho}|, \arg(\hat{\rho})]$ than the previously assumed values of $[0.5, 360^\circ]$ [18]. Consequently, U-spin breaking effects manifest themselves as a considerable asymmetry between $K_S^0\pi^+\pi^-$ and $K_L^0\pi^+\pi^-$ fit fractions of CP resonant modes like $\omega(782)$.

Furthermore, model-predicted strong-phase parameter differences between $K_S^0\pi^+\pi^-$ and $K_L^0\pi^+\pi^-$ (Δc_i^{pred} and Δs_i^{pred}) are calculated and are presented in figure 10 with a comparison with the values used in the model-independent strong-phase measurement from BESIII [18]. The values are also given in table 25 in appendix E. The uncertainties on the model-predictions from this analysis include both statistical and systematic uncertainties. The uncertainties on the assumed values in the model-independent analysis are determined by smearing the r values in a Gaussian distribution with 0.5 standard deviation about a mean of unity and δ values uniformly in the full range. Additionally, difference between the BABAR 2005 and Belle 2010 $K_S^0\pi^+\pi^-$ models are also included, both of which consider the same CP intermediate resonances in the decay described with Breit-Wigner functions for both P and S waves, under $SU(3)$ flavour symmetry assumption. This results in smaller uncertainties on the assumed values in bins 1 and 3, which contain major contributions from the $\rho(770)$ and $\pi\pi$ S-wave intermediate states. The predicted values in these bins carry uncertainties from the U-spin breaking parameters. The uncertainties in the rest of the bins are reduced as compared with the assumed values, which will result in reducing the systematic uncertainty related to the U-spin assumption in future determinations of (c_i, s_i) .

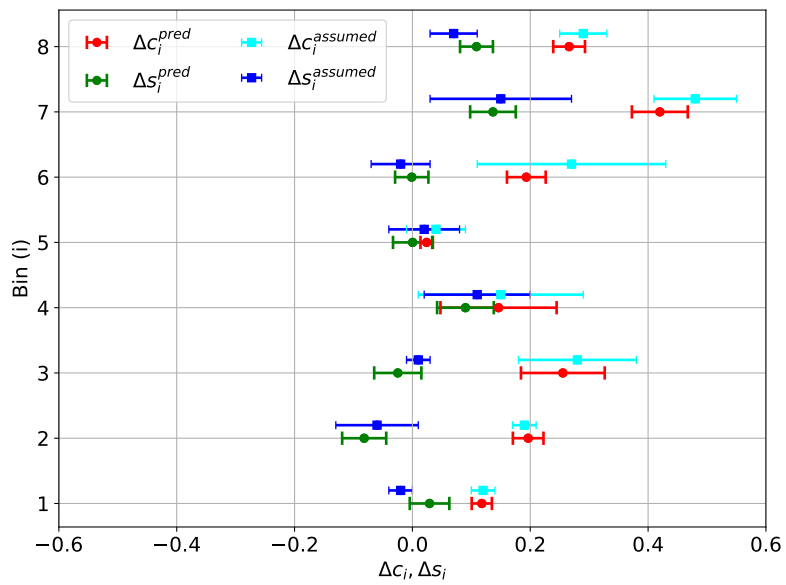


Figure 10: Model-predicted strong-phase parameter differences compared with the assumed values in the model-independent analysis from BESIII [18].

A Angular dependence of Breit-Wigner amplitude in $D \rightarrow PV$ decays

For reactions of type $D \rightarrow (ab)_r c$ and with spin transfer $0 \rightarrow j + l$, where l ($= j$) is the three-dimensional orbital angular momentum of the spectator particle, the angular part of the amplitude reduces to the expressions given in eqs. A.1, A.2 and A.3.

$$\mathcal{Z}_{L=0} = 1, \tag{A.1}$$

$$\mathcal{Z}_{L=1} = M_{bc}^2 - M_{ac}^2 - \frac{(M_D^2 - M_c^2)(M_b^2 - M_a^2)}{M_{ab}^2}, \tag{A.2}$$

$$\mathcal{Z}_{L=2} = a_1^2 - \frac{1}{3}a_2^2 a_3^2, \tag{A.3}$$

where,

$$a_1 = \mathcal{Z}_{L=1}, \text{ and}$$

$$a_{2(3)} = M_{ab}^2 - 2M_{D(a)}^2 - 2M_{c(b)}^2 + \frac{(M_{D(a)}^2 - M_{c(b)}^2)^2}{M_{ab}^2},$$

and M_{ij} denotes invariant mass of the two-particle system ij .

B Fits performed on individual tag-mode event samples separately

U-spin breaking parameter results obtained upon fitting each of the three tag-mode events separately to the corresponding amplitude function are presented along with their residuals, $(x_{\text{tot}} - x_{\text{sep}})/(\sigma(x_{\text{tot}}) + \sigma(x_{\text{sep}}))$, where x_{tot} are the fit parameters from the main fit using all the tag modes and x_{sep} are from the individual fits on the three tag-mode events.

Resonance	r	Residual	δ (deg.)	Residual
$\rho(770)$	2.23 ± 0.63	0.33	-106.20 ± 11.65	0.89
$\omega(782)$	7.93 ± 3.59	0.41	-19.26 ± 25.86	0.65
$f_2(1270)$	4.44 ± 2.07	0.23	-86.57 ± 35.95	0.57
$\rho(1450)$	17.77 ± 5.99	0.63	50.32 ± 23.41	0.74
$\pi\pi$ S-wave	0.29 ± 0.67	0.09	-188.8 ± 55.12	0.75

Table 11: U-spin breaking parameter values from individual fit on $K\pi$ tag mode events.

Resonance	r	Residual	δ (deg.)	Residual
$\rho(770)$	2.49 ± 0.53	0.70	-79.94 ± 8.36	0.75
$\omega(782)$	5.31 ± 1.27	0.40	-13.61 ± 14.93	0.72
$f_2(1270)$	2.30 ± 1.95	0.51	-44.04 ± 21.88	0.32
$\rho(1450)$	7.83 ± 4.07	0.61	118.5 ± 39.04	0.75
$\pi\pi$ S-wave	0.47 ± 0.56	0.13	-111.8 ± 58.83	0.70

Table 12: U-spin breaking parameter values from individual fit on $K\pi\pi\pi$ tag mode events.

Resonance	r	Residual	δ (deg.)	Residual
$\rho(770)$	1.52 ± 0.40	0.61	-82.57 ± 10.58	0.49
$\omega(782)$	6.86 ± 0.97	0.42	14.38 ± 7.61	0.83
$f_2(1270)$	4.54 ± 1.22	0.37	-42.07 ± 16.59	0.43
$\rho(1450)$	9.45 ± 2.74	0.47	78.05 ± 19.45	0.01
$\pi\pi$ S-wave	0.72 ± 0.38	0.59	-206.90 ± 35.53	0.83

Table 13: U-spin breaking parameter values from individual fit on $K\pi\pi^0$ tag mode events.

C Standalone $K_L^0\pi^+\pi^-$ fit

An amplitude fit is performed on the $K_L^0\pi^+\pi^-$ data events alone without using any constraint related to the $K_S^0\pi^+\pi^-$ amplitude. To avoid redundancy, no U-spin breaking parameters (r_k, δ_k) are multiplied to the CP eigenstate amplitudes as separate fit parameters, except for the reference $\rho(770)$ and the $\pi\pi$ S-wave since they are as usual kept fixed in the fit. The fixed and floated U-spin breaking parameters are given in table 14 and the resultant fit fractions and their comparison with the ones from the main fit are given in table 15.

Resonance	Simultaneous fit results (r, δ)	$K_L^0\pi^+\pi^-$ -only fit results (r, δ)
$\rho(770)$	$1.93 \pm 0.27, -90.61 \pm 5.83$	$1.93 \pm 1.10, -99.9 \pm 22.9$
$\omega(782)$	$6.13 \pm 0.75, 2.24 \pm 6.99$	1.0, 0.0 (fixed)
$f_2(1270)$	$3.75 \pm 0.90, -56.52 \pm 16.84$	1.0, 0.0 (fixed)
$\rho(1450)$	$12.12 \pm 2.92, 78.37 \pm 14.36$	1.0, 0.0 (fixed)
$\pi\pi$ S-wave	$0.37 \pm 0.21, -164.36 \pm 15.69$	$0.91 \pm 0.99, -127.6 \pm 61.9$

Table 14: U-spin breaking parameter values from a standalone fit.

Resonance	$K_L^0\pi^+\pi^-$ FF(%) (Simultaneous fit)	$K_L^0\pi^+\pi^-$ FF(%) (Standalone $K_L^0\pi^+\pi^-$)
$\rho(770)$	$18.16^{+0.53}_{-0.45}$	18.94 ± 1.20
$\omega(782)$	$0.06^{+0.03}_{-0.02}$	0.06 ± 0.03
$f_2(1270)$	0.40 ± 0.08	0.36 ± 0.08
$\rho(1450)$	0.42 ± 0.08	0.43 ± 0.10
$K^*(892)^-$	$56.98^{+0.58}_{-0.56}$	57.1 ± 1.65
$K_2^*(1430)^-$	$1.64^{+0.10}_{-0.09}$	1.58 ± 0.15
$K^*(1680)^-$	$0.25^{+0.06}_{-0.05}$	0.22 ± 0.11
$K^*(1410)^-$	0.19 ± 0.06	0.11 ± 0.06
$K^*(892)^+$	0.45 ± 0.05	0.37 ± 0.06
$K_2^*(1430)^+$	0.05 ± 0.02	0.02 ± 0.02
$K^*(1410)^+$	0.04 ± 0.02	0.02 ± 0.02
$K_0^*(1430)^-$	$6.84^{+0.24}_{-0.25}$	5.80 ± 0.38
$\pi\pi$ S-wave	$10.12^{+0.32}_{-0.33}$	10.39 ± 1.72
Total FF	$95.59^{+2.16}_{-2.07}$	95.40 ± 5.58

Table 15: $D^0 \rightarrow K_L^0\pi^+\pi^-$ fit fractions from a standalone fit.

D Systematic source-wise break up

	Source
I	Acceptance
II	Resonance masses and widths, fixed LASS parameters, and tag-side strong-phase parameters
III	Radii of resonance and D meson
IV	Peaking background fraction
V	Non-peaking background shape
VI	K-matrix coupling (β) and production parameters (f_{prod})

Table 16: Nomenclature for systematic sources.

Resonance	r	I	II	III	IV	V	VI
$\rho(770)$	1.93 ± 0.27	0.15	0.98	0.07	0.004	0.04	1.18
$\omega(782)$	6.13 ± 0.75	0.13	0.57	0.15	0.005	0.01	0.36
$f_2(1270)$	3.75 ± 0.90	0.22	0.39	0.07	0.002	0.01	0.78
$\rho(1450)$	12.12 ± 2.92	0.11	0.52	0.12	0.001	0.004	0.34
$\pi\pi$ S-wave	0.37 ± 0.21	0.19	1.02	0.04	0.004	0.00	1.43

Table 17: Systematic uncertainties in units of statistical uncertainties on U-spin breaking parameters r .

Resonance	δ (deg.)	I	II	III	IV	V	VI
$\rho(770)$	-90.61 ± 5.83	0.63	0.70	0.23	0.003	0.10	0.87
$\omega(782)$	2.24 ± 6.99	0.01	0.50	0.04	0.003	0.05	0.47
$f_2(1270)$	-56.52 ± 16.84	0.05	0.59	0.21	0.001	0.04	0.44
$\rho(1450)$	78.37 ± 14.36	0.18	0.92	0.13	0.001	0.04	0.53
$\pi\pi$ S-wave	-164.36 ± 15.69	0.43	0.62	0.05	0.003	0.03	0.40

Table 18: Systematic uncertainties in units of statistical uncertainties on U-spin breaking parameters δ .

Resonance	$K_S^0\pi^+\pi^-$ FF(%)	I	II	III	IV	V	VI
$\rho(770)$	18.90 ± 0.42	1.21	0.54	0.43	0.0003	0.07	2.80
$\omega(782)$	0.54 ± 0.09	0.11	0.38	0.34	0.001	0.00	0.67
$f_2(1270)$	$0.61^{+0.13}_{-0.11}$	0.40	0.32	0.48	0.004	0.00	1.20
$\rho(1450)$	0.21 ± 0.10	0.16	0.64	0.72	0.001	0.08	2.4
$K^*(892)^-$	$62.18^{0.55}_{-0.59}$	0.37	0.02	0.51	0.001	0.04	3.58
$K_2^*(1430)^-$	1.79 ± 0.09	0.20	0.01	0.30	0.0001	0.80	3.90
$K^*(1680)^-$	0.27 ± 0.06	2.33	2.86	2.17	0.0003	0.17	3.00
$K^*(1410)^-$	0.21 ± 0.06	0.33	1.86	0.17	0.001	0.17	0.67
$K^*(892)^+$	0.49 ± 0.05	1.00	2.00	0.50	0.005	0.50	3.00
$K_2^*(1430)^+$	0.05 ± 0.02	0.00	0.22	0.00	0.006	0.50	1.00
$K^*(1410)^+$	0.05 ± 0.03	0.00	0.18	0.00	0.002	0.33	0.33
$K_0^*(1430)^-$	7.47 ± 0.26	0.3	0.86	0.46	0.0003	0.04	4.29
$\pi\pi$ S-wave	10.24 ± 0.23	0.58	0.74	0.83	0.0004	0.17	4.71

Table 19: Systematic uncertainties in units of statistical uncertainties on $K_S^0\pi^+\pi^-$ fit fractions.

Resonance	$K_L^0 \pi^+ \pi^-$ FF(%)	I	II	III	IV	V	VI
$\rho(770)$	$18.16^{+0.53}_{-0.45}$	0.38	1.02	0.66	0.0004	0.51	2.53
$\omega(782)$	0.06 ± 0.025	0.00	0.40	0.92	0.002	0.00	0.40
$f_2(1270)$	0.40 ± 0.08	0.53	1.16	0.40	0.006	0.27	2.27
$\rho(1450)$	0.42 ± 0.08	0.50	1.93	1.00	0.004	0.12	3.12
$K^*(892)^-$	$56.98^{+0.58}_{-0.56}$	0.82	1.68	0.44	0.003	0.93	1.57
$K_2^*(1430)^-$	$1.64^{+0.10}_{-0.09}$	0.00	0.67	0.21	0.0005	0.53	3.68
$K^*(1680)^-$	$0.25^{+0.06}_{-0.05}$	2.36	2.67	2.18	0.0001	1.82	3.27
$K^*(1410)^-$	0.19 ± 0.06	0.33	1.93	0.17	0.001	0.17	5.00
$K^*(892)^+$	0.45 ± 0.05	0.40	0.80	0.20	0.005	0.20	1.20
$K_2^*(1430)^+$	0.05 ± 0.02	0.50	0.21	0.00	0.005	0.50	1.00
$K^*(1410)^+$	0.04 ± 0.02	0.00	0.51	0.00	0.004	0.50	0.50
$K_0^*(1430)^-$	$6.84^{+0.24}_{-0.25}$	0.65	1.37	0.49	0.001	0.78	4.20
$\pi\pi$ S-wave	$10.12^{+0.32}_{-0.33}$	0.37	0.68	0.25	0.004	0.18	1.46

Table 20: Systematic uncertainties in units of statistical uncertainties on $K_L^0 \pi^+ \pi^-$ fit fractions.

Bin	c_i	I	II	III	IV	V	VI
1	0.695 ± 0.007	0.00	1.30	0.62	0.003	0.18	1.22
2	0.614 ± 0.010	0.39	1.32	0.57	0.002	0.65	1.28
3	0.038 ± 0.027	0.46	2.66	0.37	0.001	0.46	2.24
4	-0.542 ± 0.027	0.39	0.97	0.24	0.001	0.41	2.70
5	-0.947 ± 0.004	0.11	1.85	0.51	0.012	0.06	2.92
6	-0.494 ± 0.020	1.21	0.98	0.21	0.0005	0.007	1.98
7	0.114 ± 0.026	0.67	1.52	0.40	0.002	0.17	1.90
8	0.453 ± 0.015	0.48	1.87	0.41	0.003	0.10	2.18

Table 21: Systematic uncertainties in units of statistical uncertainties on c_i .

Bin	s_i	I	II	III	IV	V	VI
1	0.021 ± 0.014	0.82	0.75	0.64	0.001	0.15	1.64
2	0.408 ± 0.013	0.75	1.09	0.84	0.002	0.15	1.95
3	0.831 ± 0.006	1.02	1.82	0.08	0.002	0.37	2.55
4	0.719 ± 0.020	0.27	0.57	0.37	0.001	0.40	2.56
5	-0.052 ± 0.020	0.06	0.85	0.24	0.001	0.03	2.08
6	-0.644 ± 0.012	0.28	0.52	0.51	0.002	0.13	2.29
7	-0.805 ± 0.014	1.51	0.97	0.73	0.001	0.17	1.14
8	-0.441 ± 0.021	1.02	0.37	0.72	0.001	0.04	1.42

Table 22: Systematic uncertainties in units of statistical uncertainties on s_i .

Bin	c'_i	I	II	III	IV	V	VI
1	0.797 ± 0.006	0.69	1.39	0.52	0.002	1.14	1.23
2	0.812 ± 0.007	0.23	1.22	0.42	0.005	0.24	1.51
3	0.292 ± 0.025	0.46	0.84	0.49	0.002	0.30	1.19
4	-0.392 ± 0.027	0.34	0.70	0.36	0.001	0.26	1.32
5	-0.923 ± 0.005	0.13	2.61	0.67	0.002	2.49	3.72
6	-0.300 ± 0.020	1.21	1.01	0.36	0.002	0.77	2.39
7	0.541 ± 0.020	2.50	2.77	0.32	0.003	0.11	2.66
8	0.726 ± 0.010	2.24	2.14	0.50	0.003	0.26	2.49

Table 23: Systematic uncertainties in units of statistical uncertainties on c'_i .

Bin	s'_i	I	II	III	IV	V	VI
1	0.044 ± 0.014	1.20	0.90	0.40	0.002	0.81	1.55
2	0.327 ± 0.014	0.60	1.58	0.52	0.004	0.19	1.72
3	0.806 ± 0.010	0.13	1.88	0.36	0.004	0.08	1.93
4	0.811 ± 0.015	0.48	0.56	0.43	0.001	0.85	2.02
5	-0.045 ± 0.040	0.03	0.74	0.21	0.001	0.27	1.63
6	-0.641 ± 0.013	0.26	0.84	0.49	0.002	0.18	1.85
7	-0.663 ± 0.028	0.66	1.58	0.64	0.002	0.83	1.88
8	-0.327 ± 0.020	1.21	0.38	0.54	0.002	0.27	1.62

Table 24: Systematic uncertainties in units of statistical uncertainties on s'_i .

E Predicted and assumed $\Delta c_i, \Delta s_i$

Bin	$\Delta c_i \pm \delta\Delta c_i$ [predicted]	$\Delta s_i \pm \delta\Delta s_i$ [predicted]	$\Delta c_i \pm \delta\Delta c_i$ [assumed]	$\Delta s_i \pm \delta\Delta s_i$ [assumed]
1	0.12 ± 0.02	0.03 ± 0.03	0.12 ± 0.02	-0.02 ± 0.02
2	0.20 ± 0.02	-0.08 ± 0.04	0.19 ± 0.02	-0.06 ± 0.07
3	0.26 ± 0.07	-0.02 ± 0.04	0.28 ± 0.10	0.01 ± 0.02
4	0.15 ± 0.10	0.09 ± 0.05	0.15 ± 0.14	0.11 ± 0.09
5	0.02 ± 0.01	0.00 ± 0.03	0.04 ± 0.05	0.02 ± 0.06
6	0.19 ± 0.03	0.00 ± 0.03	0.27 ± 0.16	-0.02 ± 0.05
7	0.42 ± 0.05	0.14 ± 0.04	0.48 ± 0.07	0.15 ± 0.07
8	0.27 ± 0.03	0.11 ± 0.03	0.29 ± 0.04	0.07 ± 0.04

Table 25: Model-predicted and previously assumed strong-phase parameter differences ($\Delta c_i, \Delta s_i$). Uncertainties on the predicted values include both statistical and systematic.

Acknowledgement

The BESIII collaboration thanks the staff of BEPCII and the IHEP computing center for their strong support. This work is supported in part by National Key R&D Program of China under Contracts Nos. 2020YFA0406300, 2020YFA0406400; National Natural Science Foundation of China (NSFC) under Contracts Nos. 11635010, 11735014, 11835012, 11935015, 11935016, 11935018, 11961141012, 12022510, 12025502, 12035009, 12035013, 12061131003, 12192260, 12192261, 12192262, 12192263, 12192264, 12192265; the Chinese Academy of Sciences (CAS) Large-Scale Scientific Facility Program; the CAS Center for Excellence in Particle Physics (CCEPP); Joint Large-Scale Scientific Facility Funds of the NSFC and CAS under Contract No. U1832207; CAS Key Research Program of Frontier Sciences under Contracts Nos. QYZDJ-SSW-SLH003, QYZDJ-SSW-SLH040; 100 Talents Program of CAS; The Institute of Nuclear and Particle Physics (INPAC) and Shanghai Key Laboratory for Particle Physics and Cosmology; ERC under Contract No. 758462; European Union's Horizon 2020 research and innovation programme under Marie Skłodowska-Curie grant agreement under Contract No. 894790; German Research Foundation DFG under Contracts Nos. 443159800, 455635585, Collaborative Research Center CRC 1044, FOR5327, GRK 2149; Istituto Nazionale di Fisica Nucleare, Italy; Ministry of Development of Turkey under Contract No. DPT2006K-120470; National Science and Technology fund; National Science Research and Innovation Fund (NSRF) via the Program Management Unit for Human Resources & Institutional Development, Research and Innovation under Contract No. B16F640076; Olle Engkvist Foundation under Contract No. 200-0605; STFC (United Kingdom); Suranaree University of Technology (SUT), Thailand Science Research and Innovation (TSRI), and National Science Research and Innovation Fund (NSRF) under Contract No. 160355; The Royal Society, UK under Contracts Nos. DH140054, DH160214; The Swedish Research Council; U. S. Department of Energy under Contract No. DE-FG02-05ER41374

References

- [1] N. Cabibbo, *Unitary Symmetry and Leptonic Decays*, *Phys. Rev. Lett.* **10**, 531 (1963).
- [2] M. Kobayashi and T. Maskawa, *CP-violation in the Renormalizable Theory of Weak Interactions*, *Prog. Theor. Exp. Phys.*, **49(2)**, 652 (1973).
- [3] M. Gronau and D. Wyler, *On determining a weak phase from CP asymmetries in charged B decays*, *Phys. Lett. B* **265**, 172-176 (1991).
- [4] D. Atwood, I. Dunietz, and A. Soni, *Enhanced CP violation with $B \rightarrow KD^0(\bar{D}^0)$ modes and extraction of the CKM angle γ* , *Phys. Rev. Lett.* **78**, 3257 (1997), [arXiv:hep-ph/9612433](#).
- [5] D. Atwood, I. Dunietz, and A. Soni, *Improved methods for observing CP violation in $B^\pm \rightarrow KD$ and measuring the CKM phase γ* , *Phys. Rev. D* **63**, 036005 (2001), [arXiv:hep-ph/0008090](#).
- [6] J. Brod and J. Zupan, *The ultimate theoretical error on γ from $B \rightarrow DK$ decays*, *J. High Energ. Phys.* **1401**, 051 (2014), [arXiv:1308.5663](#).
- [7] J. Brod, A. Lenz, G. Tetlalmatzi-Xolocotzi and M. Wiebusch, *New physics effects in tree-level decays and the precision in the determination of the quark mixing angle γ* , *Phys. Rev. D* **92**, 033002 (2015), [arXiv:1412.1446](#).
- [8] A. Giri, Y. Grossman, A. Soffer, and J. Zupan, *Determining γ using $B^\pm \rightarrow DK^\pm$ with multibody D decays*, *Phys. Rev. D* **68**, 054018 (2003).
- [9] A. Bondar. *Proceedings of BINP special analysis meeting on Dalitz analysis*, 24–26 Sep. 2002, unpublished.
- [10] The LHCb collaboration, *Measurement of the CKM angle γ in $B^\pm \rightarrow DK^\pm$ and $B^\pm \rightarrow D\pi^\pm$ decays with $D \rightarrow K_S^0 h^+ h^-$* , *J. High Energ. Phys.* **2102**, 169 (2021), [arXiv:2010.08483](#).
- [11] The Belle and Belle II collaborations, *Combined analysis of Belle and Belle II data to determine the CKM angle ϕ_3 using $B^+ \rightarrow D(K_S^0 h^+ h^-)h^+$* , *J. High Energ. Phys.* **2022**, 63 (2022), [arXiv:2110.12125](#).
- [12] A. Bondar and A. Poluektov, *The use of quantum-correlated D^0 decays for ϕ_3 measurement*, *Eur. Phys. J. C* **55**, 51 (2008).
- [13] D. Atwood and A. Soni, *Role of a charm factory in extracting CKM-phase information via $B \rightarrow DK$* , *Phys. Rev. D* **68**, 033003 (2003).
- [14] The Belle collaboration, *Measurement of CKM angle ϕ_1 in $B^0 \rightarrow \bar{D}^{(*)0} h^0$, $\bar{D}^0 \rightarrow K_S^0 \pi^+ \pi^-$ decays with time-dependent binned Dalitz plot analysis*, *Phys. Rev. D* **94**, 052004 (2016).
- [15] BABAR and Belle collaborations, *Measurement of $\cos 2\beta$ in $B^0 \rightarrow D^{(*)} h^0$ with $D \rightarrow K_S^0 \pi^+ \pi^-$ decays by a combined time-dependent Dalitz plot analysis of BABAR and Belle data*, *Phys. Rev. D* **98**, 112012 (2018).
- [16] The LHCb collaboration, *Observation of the Mass Difference between Neutral Charm-Meson Eigenstates*, *Phys. Rev. Lett.* **127**, 111801 (2021).
- [17] The BESIII collaboration, *Design and construction of the BESIII detector*, *Nucl. Instrum. Meth. A* **614**, 345 (2010), [arXiv:0911.4960](#).
- [18] The BESIII collaboration, *Model-independent determination of the relative strong-phase difference between D^0 and $\bar{D}^0 \rightarrow K_{S/L}^0 \pi^+ \pi^-$ and its impact on the measurement of the CKM angle γ/ϕ_3* , *Phys. Rev. D* **101**, 112002 (2020).

- [19] The BESIII collaboration, *Determination of strong-phase parameters in $D \rightarrow K_{S/L}^0 \pi^+ \pi^-$* , [Phys. Rev. Lett. **124**, 241802 \(2020\)](#).
- [20] The CLEO collaboration, *Model independent determination of the strong-phase difference between D^0 and $\bar{D}^0 \rightarrow K_{S/L}^0 h^+ h^-$ ($h = \pi, K$) and its impact on the measurement of the CKM angle γ/ϕ_3* , [Phys. Rev. D **82**, 112006 \(2010\)](#).
- [21] The Particle Data Group collaboration, *Review of particle physics*, [Prog. Theor. Exp. Phys. **2020**, 083C01 \(2020\)](#).
- [22] F. Hippel and C. Quigg, *Centrifugal-Barrier Effects in Resonance Partial Decay Widths, Shapes, and Production Amplitudes*, [Phys. Rev. D **5**, 624 \(1972\)](#).
- [23] J. M. Blatt and V. F. Weisskopf, *Theoretical Nuclear Physics* (John Wiley and Sons, New York, 1952).
- [24] S. U. Chung, *Spin Formalisms*, [CERN Yellow Report CERN-71-08, 81p \(1971\)](#).
- [25] S. U. Chung, *General formulation of covariant helicity-coupling amplitudes*, [Phys. Rev. D **57**, 431 \(1998\)](#).
- [26] V. Filippini, A. Fontana and A. Rotondi, *Covariant spin tensors in meson spectroscopy*, [Phys. Rev. D **51**, 2247 \(1995\)](#).
- [27] B. S. Zou and D. V. Bugg, *Covariant tensor formalism for partial-wave analyses of ψ decay to mesons*, [Eur. Phys. J. A **16**, 537 \(2003\)](#).
- [28] S. U. Chung *et al.*, *Partial wave analysis in K-matrix formalism*, [Annalen Phys. **4**, 404 \(1995\)](#).
- [29] V. V. Anisovich and A. V. Sarantsev, *K-matrix analysis of the ($IJ^{PC} = 00^{++}$)-wave in the mass region below 1900 MeV*, [Eur. Phys. J. A **16**, 229 \(2003\)](#), [arXiv:hep-ph/0204328](#).
- [30] The FOCUS collaboration, *Dalitz plot analysis of the $D^+ \rightarrow K^- \pi^+ \pi^+$ decay in the FOCUS experiment*, [Phys. Lett. B, **653**, 1 \(2007\)](#), [arXiv:0705.2248](#).
- [31] D. Aston *et al.*, *Study of $K\pi$ scattering in the reaction $K^- p \rightarrow K^- \pi^+ n$ at 11 GeV/c*, [Nucl. Phys. B **296**, 493 \(1988\)](#).
- [32] I. I. Bigi and H. Yamamoto, *Interference between Cabibbo allowed and doubly forbidden transitions in $D \rightarrow K_{S,L} + \pi'$ s decays*, [Phys. Lett. B. **349**, 363 \(1995\)](#), [arXiv:hep-ph/9502238](#).
- [33] C. H. Yu *et al.*, *BEPCII Performance and Beam Dynamics Studies on Luminosity*, [Proceedings of IPAC \(2016\), TUYA01](#).
- [34] The BESIII Collaboration, *Future Physics Programme of BESIII*, [Chin. Phys. C **44**, 040001 \(2020\)](#).
- [35] S. Jadach, B.F.L. Ward, Z. Was, *The Precision Monte Carlo Event Generator KK For Two-Fermion Final States In e^+e^- Collisions*, [Comput. Phys. Commun. **130**, 260 \(2000\)](#).
- [36] PING Rong-Gang *et al.*, *An exclusive event generator for e^+e^- scan experiments*, [Chinese Phys. C **38**, 083001 \(2014\)](#).
- [37] GEANT4 collaboration, *Geant4 — a simulation toolkit*, [Nucl. Instrum. Meth. A **506**, 250 \(2003\)](#).
- [38] The ARGUS collaboration, *Search for hadronic $b \rightarrow u$ decays*, [Phys. Lett. B **241**, 278 \(1990\)](#).
- [39] S. Masashi, *Numerical Approximation of Predictive Distribution: Introduction to Statistical Machine Learning*, [Elsevier, 2016, pp. 205-214](#).

- [40] K. S. Cranmer, *Kernel estimation in high-energy physics*, *Comput. Phys. Commun.* **136**, 198 (2001), [arXiv:hep-ex:0011057](#).
- [41] The LHCb collaboration, *Simultaneous determination of CKM angle γ and charm mixing parameters*, *J. High Energ. Phys.* **2021**, 141 (2021).
- [42] The BESIII collaboration, *Measurement of the $D \rightarrow K^- \pi^+ \pi^+ \pi^-$ and $D \rightarrow K^- \pi^+ \pi^0$ coherence factors and average strong-phase differences in quantum-correlated $D\bar{D}$ decays*, *J. High Energ. Phys.* **2021**, 164 (2021).
- [43] S. S. Wilks, *The Large-Sample Distribution of the Likelihood Ratio for Testing Composite Hypotheses*, *Ann. Math. Statist.* **9(1)**, 60 (1938).
- [44] G. J. Gounaris and J. J. Sakurai, *Finite-Width Corrections to the Vector-Meson-Dominance Prediction for $\rho \rightarrow e^+ e^-$* , *Phys. Rev. Lett.* **21**, 244 (1968).
- [45] M. Nayak *et al.*, *First determination of CP content of $D \rightarrow \pi^+ \pi^- \pi^0$ and $D \rightarrow K^+ K^- \pi^0$* , *Phys. Lett. B.* **740**, 1 (2015).